Nanoscale characteristics of a room-temperature coexisting phase of magnetic skyrmions and antiskyrmions for skyrmion-antiskyrmion-based spintronic applications

Daigo Shimizu[1*], Tomoki Nagase[1], Yeong-Gi So[2], Makoto Kuwahara[3], Nobuyuki Ikarashi[1,4], and Masahiro Nagao[1,4*]

1 Department of Electronics, Nagoya University, Nagoya 464-8603, Japan

2 Department of Materials Science, Akita University, Akita 010-8502, Japan

3 Advanced Measurement Technology Center, Institute of Materials and Systems for Sustainability, Nagoya University, Nagoya 464-8601, Japan

4 Center for Integrated Research of Future Electronics, Institute of Materials and Systems for Sustainability, Nagoya University, Nagoya 464-8601, Japan

KEYWORDS: *skyrmions, antiskyrmions, Heusler materials, Lorentz transmission electron microscopy, micromagnetic simulations*

ABSTRACT:

Theoretical studies have predicted that interactions between magnetic skyrmions and antiskyrmions give rise to various properties, such as unique arrangements, pair annihilation, topological transformation, and rectilinear and trochoidal motions that do not appear in only skyrmions or antiskyrmions. Recently, experimental studies have discovered that a Heusler material with the anisotropic Dzyaloshinskii-Moriya interaction shows a coexisting phase at 268 K and in-plane magnetic field-induced topological transformation of elliptical skyrmions and square-shaped antiskyrmions. Therefore, experimentally observed the coexisting phase and the topological transformation could be promising for developing skyrmion-antiskyrmion-based spintronics. However, such interactions and the detailed transformation mechanism remain unrevealed and unclear, respectively. Using Lorentz transmission electron microscopy experiments and micromagnetic simulations, we comprehensively study the properties in a coexisting phase of skyrmions and antiskyrmions in a Heusler material, $Mn_{1.3}Pt_{1.0}Pd_{0.1}Sn$. Control of dipolar interaction (the sample thickness) allows us to realize a room-temperature coexisting phase. We find that the topological transformation occurs stochastically rather than deterministically, which can be explained by considering the magnetic point group and the direction of an in-plane magnetic field. We further observe isotropic long-range repulsive interaction between skyrmions and antiskyrmions in contrast to conventional thought of the relative-position- and helicity-dependent short-range pairwise interactions, and deformation of skyrmions and antiskyrmions depending on the distance between them. Our simulations show that the deformation exerts significant influence on the magnetic energies and the energy landscape, contributing to the interaction. Our results provide insight into coexisting phases of

skyrmions and antiskyrmions and a guide for developing skyrmion-antiskyrmion-based spintronics.

INTRODUCTION

Skyrmions have been ubiquitous in condensed matter, whereas antiskyrmions rarely exist alone. In magnets, experiments have directly observed skyrmions and antiskyrmions as single phases, respectively,[1,2] that offer appealing platforms to explore emergent electromagnetic fields and related properties. Magnetic skyrmions and antiskyrmions are non-coplanar spin structures with opposite topological charges.[3] Skyrmions are stabilized by Dzyaloshinskii-Moriya interaction (DMI) originating from spatial inversion symmetry breaking of the systems such as chiral magnets[1,4-6] with T, O, C_{3v} symmetries and asymmetric magnetic multilayers.[7] On the other hand, antiskyrmions have been observed in Heusler materials, Mn-Pt(-Pd)-Sn,[2,8-17] with D_{2d} symmetry (Figure 1a) and a schreibersite, $Fe_{1.9}Ni_{0.9}Pd_{0.2}P$,[18] with S_4 symmetry. These symmetries lead to anisotropic DMI.

Of particular interest are coexisting phases of magnetic skyrmions and antiskyrmions, where recent many theories have proposed a variety of fascinating properties[3,19-25] owing to interactions that do not appear in every single phase. Examples include skyrmion-antiskyrmion liquid,[19] a rectangular lattice with alternating columns of skyrmions and antiskyrmions,[20] phase separation,[21,22] current-induced pair annihilation that emits propagating spin wave,[23] topological conversions by their collision,[3,23,24] and rectilinear and trochoidal motions of skyrmions and antiskyrmions, respectively.[25] Experimentally elucidating and understanding such underlying interactions are thus a research challenge in condensed-matter physics. Materials with

anisotropic Dzyaloshinskii-Moriya interaction (DMI), such as a Heusler material and schreibersite, could offer a unique opportunity for investigating interactions. Recent Lorentz transmission electron microscopy (L-TEM) experiments have first discovered the coexisting phase at T_{CO} ~268 K in a Heusler material[12] and at room temperature in a schreibersite.[18]

In the thin films of the Heusler material and schreibersite, other L-TEM experiments have demonstrated a topological transformation between square-shaped antiskyrmions and elliptical Bloch skyrmions with clockwise (CW) and anticlockwise (ACW) via the non-topological (NT) bubbles by in-plane magnetic fields, as the following procedure.[11,13] The sample tilt angle θ is defined as the angle of the incident electron beam (parallel to magnetic fields) away from the tetragonal [001] crystal zone axis, and the rotation axis is the [100] direction. When the sample tilts away from $\theta = \sim 0°$ where square-shaped antiskyrmions are observed, an in-plane component of the magnetic field induces bullet-shaped NT-bubbles with two Bloch lines, and then back to $\theta = \sim 0°$, NT-bubbles convert to elliptical Bloch skyrmions with either CW or ACW depending on the rotation axes. The discoveries of the coexisting phase and the topological transformations could make materials with anisotropic DMI a platform for developing skyrmion-antiskyrmion-based spintronics, such as a racetrack memory which is expected to have higher reliability by the assignment of skyrmions and antiskyrmions to the information carriers respectively, compared to skyrmion-based that.[13,26] However, in such materials, the detailed transformation mechanism and the skyrmion-antiskyrmion interaction governing the dynamic properties[27,28] remain unrevealed.

In this study, we have focused on the coexisting phases of skyrmions and antiskyrmions in the thin film of a Heusler material, $Mn_{1.3}Pt_{1.0}Pd_{0.1}Sn$. We have used L-TEM experiments and micromagnetic simulations to comprehensively characterize the properties of the coexisting

phase. As a result, we have realized a room-temperature (RT) coexisting phase, revealed the transformation mechanism, and found new physical properties in the coexisting phase. We show a room-temperature coexisting phase at the sample thickness of t ~100 nm, resulting from an appropriate degree of competition between the DMI and dipolar interaction.[18] In addition to realizing the room-temperature coexisting phase, we find the stochastic topological transformation between skyrmions and antiskyrmions through NT-bubbles, which can be explained by considering the magnetic point group and the direction of an in-plane magnetic field for the NT bubble. Furthermore, we experimentally observe signatures of isotropic long-range repulsive interaction (force) between and among skyrmions and antiskyrmions accompanied by their deformation depending on the distance between them. Micromagnetic simulations support the experimental interpretation and suggest that the deformed skyrmions and antiskyrmions significantly affect the energy behaviors and the energy landscape, contributing to repulsive interaction.

RESULTS AND DISCUSSION

For our study, we synthesized a bulk polycrystalline sample of tetragonal inverse Heusler material $Mn_{1.3}Pt_{1.0}Pd_{0.1}Sn$. An alloy ingot was prepared from high-purity Mn (99.99 wt.%), Pt (99.95 wt.%), Pd (99.95 wt.%) and Sn (99.99 wt.%) via Ar arc melting. The ingot was subsequently sealed in an evacuated silica tube and annealed at 1073 K for a week, followed by water quenching.[2] The thin films for the L-TEM observations were thinned by mechanical cutting and then argon ion milling method and by focused ion beam technique. We used the Fresnel method as an L-TEM to observe the magnetic structures. The acceleration voltage of L-

TEM is operated at 200 kV and the electron current density is about 25.0 pA/cm^2 when electron beam is focused. A magnetic field was applied parallel to the incident electron beam by controlling the objective-lens current. We used L-TEM to estimate the Curie temperature (T_C) as the temperature that the contrast arising from the magnetic orders disappears as increased the temperature. We recorded the values of the temperature indication to create the phase diagrams, where the sample temperatures were measured with a thermocouple away from observed regions. The electron irradiation generally causes a slight increase in temperature at the observed region. In other words, the temperature values of the observed regions are considered to be about 10 K higher than those of the temperature indication. In L-TEM experiments, we got the magnetic states 3 minutes after the displayed temperatures reached the target ones, indicating that our data are under stationary state. In addition, we used the electron beam with the large diameter, i.e., low dose electron to suppress an increase in temperature as much as possible. We used electron energy-loss spectroscopy (EELS) to measure the sample thickness, which has an error of ± 20 nm.

Room-temperature coexisting phases are an important step for realizing the skyrmion-antiskyrmion-based spintronics. The previous study on the schreibersite[18] should be useful in realizing the room-temperature coexisting phase in the Heusler materials. The authors have demonstrated that dipolar interaction whose strength varies depending on the sample thickness favors pure Bloch skyrmions, while the anisotropic DMI favors antiskyrmions including Néel components,[18] resulting in a room-temperature coexisting phase. Based on this knowledge, the Heusler materials could also enable us to realize the room-temperature coexisting phase by controlling the sample thickness. Figures 1b,c show the temperature-magnetic field phase diagrams of $Mn_{1.3}Pt_{1.0}Pd_{0.1}Sn$ for the sample thickness of t ~150 nm and ~100 nm, respectively.

We have performed the experiments in the same way as in the previous study on $Mn_{1.4}Pt_{0.9}Pd_{0.1}Sn$.[11] The coexisting phases appear at the boundary between the low-temperature skyrmion phase and the high-temperature antiskyrmion phase, and the Curie temperature is T_C ~370 K, which are qualitatively and quantitatively the same as those in $Mn_{1.4}Pt_{0.9}Pd_{0.1}Sn$,[11] respectively. Our phase diagrams with different sample thicknesses allow us to compare the effect of dipolar interaction on skyrmions and antiskyrmions. At t ~150 nm, the coexisting phase appears over the range ΔT_{CO} = 260 K ~ 280 K (Figure 1b), while, at t ~100 nm, ΔT_{CO} = 290 K ~ 330 K (Figure 1c). Similar trends were observed in the case of $Fe_{1.9}Ni_{0.9}Pd_{0.2}P$.[18] In other words, as the sample thickness reduces from t ~150 nm to t ~100 nm, dipolar interaction enhances the stability of Bloch skyrmions, resulting in which the low-temperature skyrmion phase extends towards high temperatures at the expense of the high-temperature antiskyrmion phase. As a result, the room-temperature coexisting phase appears in our sample with t ~100 nm, as shown in the L-TEM image of Figure 1d. There are many bubbles in the upper region where bend contours (strong dark contrasts) appear. Bend contours satisfy the local Bragg condition due to sample bend, indicating that the in-plane magnetic field is insufficient for changing from NT-bubbles to skyrmions or antiskyrmions.[11] Incidentally, the difference in T_{CO} between our sample ($Mn_{1.3}Pt_{1.0}Pd_{0.1}Sn$) and $Mn_{1.4}Pt_{0.9}Pd_{0.1}Sn$, even though they are the same t ~100 nm, is attributed to the difference in the DMI strength (D). In Heusler materials, the helical period of λ is proportional to A/D at a zero magnetic field,[16] where A is the exchange stiffness constant proportional to T_C. The L-TEM experiments show λ = 200 ± 5 nm in our sample (Supporting Information (SI) Figure S2), while λ = 140 ± 15 nm in $Mn_{1.4}Pt_{0.9}Pd_{0.1}Sn$,[11] suggesting that the D of our sample is smaller than that of $Mn_{1.4}Pt_{0.9}Pd_{0.1}Sn$. The decrease in the D leads to the decrease in the temperature region of the antiskyrmion phase towards high temperatures.[18] As a

result, the T_{CO} of our sample is higher than that of $Mn_{1.4}Pt_{0.9}Pd_{0.1}Sn$. The difference in the D may result from that in chemical composition, in the same as $B20$-type chiral magnets.[29]

Although the previous studies[18,30] and our results have demonstrated that dipolar interaction favors Bloch component of the spin textures, the microscopic mechanism has been not yet clear. In general, in the case of in-plane magnetized thin films, it is well known that Néel rotational mode at domain walls are energetically lower than Bloch rotational mode due to dipolar interaction. Because the former and latter have the components of in-plane and out-of-plane rotational magnetic moments. However, in the case of out-of-plane magnetized thin films (in our sample), Néel rotational mode is energetically equivalent to Bloch one irrespective of dipolar interaction, which cannot explain our result and the previous experimental[18] and simulation results.[30] Therefore, understanding the microscopic mechanism of the dipolar interaction effect is a future issue.

We have confirmed topological transformations between antiskyrmions and skyrmions via NT-bubbles with Bloch lines in the room-temperature coexisting phase of our sample, $Mn_{1.3}Pt_{1.0}Pd_{0.1}Sn$, consistent with the previous studies.[11,18] Note that the transformations occur stochastically rather than deterministically. All of the following L-TEM experiments were performed at the direction of magnetic field parallel to the incident electron beam. We define the tilt angle as $\theta = 0°$ as the incident electron beam is parallel to the [001] direction and set that the rotation axes are in the [100] directions (Figure 2a). A slight small sample tilt generates an in-plane magnetic field. When an in-plane magnetic field is antiparallel to the magnetization component of two Bloch lines in an NT-bubble, the transformations occur stochastically. In other words, this slight angle of $\theta = \sim 0°$ is opposite in sign to $\theta = 15°$ for the creation of NT-bubbles. We refer to this in-plane magnetic field as “the negative in-plane magnetic field”. Figure 2b-f

show a series of L-TEM images at room temperature, $t \sim 100$ nm, and 380 mT. These images show the reversible transformations. Here we obtained these L-TEM images by the following procedures. We tilted the sample to $\theta = +15°$ to form the NT-bubble (Figure 2c,e) and turn back to $\theta = -2.1° \sim -2.3°$ to form the skyrmion (Figure 2d) or the antiskyrmion (Figure 2f) by the negative in-plane magnetic fields and then to $\theta = -0.6° \sim -0.8°$. The last procedure that is a change from $\theta = -2.1° \sim -2.3°$ to $\theta = -0.6° \sim -0.8°$ was to avoid local diffraction contrasts, the so-called bend contours where the Bragg condition is locally satisfied due to the sample bend, that partially cover observed local regions. We have repeated these procedures to obtain NT bubbles, square-shaped antiskyrmions, and ACW elliptical skyrmions. Note that, in Figure 2b-f, although we have extracted and included only the transformations with different topologies, those occur stochastically in reality.

The stochastic reversible transformations occur accompanied by magnetic symmetry breaking and restoration. Figure 2g displays three-dimensional magnetic point groups that the spin structures have in the order of higher symmetry from the top. Antiskyrmions, skyrmions, and NT-bubbles have magnetic point groups of –4’2’*m*, 2’2’2, and 2’, respectively. NT-bubbles, the intermediate states, have the lowest symmetry. Symmetry restoration occurs at the transformation from NT-bubbles to skyrmions (Figure 2c to d) by restoring a symmetry element of 2’, and from NT-bubbles to antiskyrmions (Figure 2e to f) by restoring that of –4’, 2’, and *m*.

The stochastic reversible transformations result from stochastically creating two Bloch lines into NT-bubble or vanishing two Bloch lines of NT-bubble by the negative in-plane magnetic field. The negative in-plane magnetic field is antiparallel to the net in-plane magnetic component of two Bloch lines in NT-bubbles, which induces symmetry restorations from NT-bubble to the skyrmion or the antiskyrmion. Figure 2h shows a schematic of the transformation from NT-

bubble (the left) with two Bloch lines (the small blue arrows) to other spin structures (the right column) by a negative in-plane magnetic field (the large red arrow denoted by B_{in}). In the experiment, we slightly tilt the sample to $\theta = -2.1° \sim -2.3°$ (Figure 2b,d,f) to induce the negative in-plane magnetic fields. When the negative in-plane magnetic field stochastically creates additional two Bloch lines (the small red arrows) of which the net in-plane component is parallel to the negative in-plane magnetic field, the antiskyrmion with four Bloch lines in NT-bubble is formed (the yellow arrow in Figure 2f and the top of the right column in Figure 2h). On the other hand, when stochastically vanishing the original two Bloch lines opposite to B_{in}, the skyrmion without any Bloch lines is formed (the yellow arrow in Figure 2d and the second of the right column in Figure 2h). When the creation and annihilation of Bloch lines simultaneously occur by B_{in}, NT-bubble changes into another NT-bubble (the black arrows in Figure 2d and the third of the right column in Figure 2h). In the other case, NT-bubble remains unchanged (the white arrow in Figure 2f and the bottom of the right column in Figure 2h). In spintronics, the realization of deterministic transformation between skyrmions and antiskyrmions requires local electrical control, of which the establishment is a future challenge.

Fundamental understanding to explore application possibilities of skyrmion-antiskyrmion-based spintronics requires knowledge of the interaction underlying the dynamics in the coexisting phase. In addition, it would be interesting in various physics fields to see whether short-range pairwise interactions between skyrmions and antiskyrmions are universal or not.[3,19,20,23] Here, to elucidate interactions, we have annihilated single spin textures by local heating as theoretically proposed[31] with a focused electron beam in a region where skyrmions and antiskyrmions coexist and then measured the displacements of the remaining spin textures driven by the interaction. Beforehand, we have confirmed the annihilation of single spin textures

by irradiating a focused electron beam with a diameter of r ~200 nm in 2 minutes. Besides, we have confirmed that the thermal current (magnon current) generated by local heating does not affect the spin textures at least 700 nm away from the local heating position (SI Figure S3).

We observe signatures of isotropic long-range repulsive interactions between skyrmions and antiskyrmions. We refer to the skyrmions, antiskyrmions, and NT-bubbles collectively as particles in this paragraph. Figure 3a,b show the particle distributions before and after the annihilation of a single spin texture by the focused electron beam with r ~200 nm in 1.5 minutes, respectively. Around the right region in Figure 3a, we had repeatedly annihilated the particles before acquiring this image, resulting in the interparticle distance of 400-550 nm. After exposing a single particle (NT-bubble) within the dotted yellow circle in Figure 3a, we confirmed the annihilation of the particle and the redistribution and displacements of the remaining particles overcoming the pinning force as shown in Figure 3b. These color arrows indicate the direction and magnitude of the particle displacements from the initial particle positions before local heating. Most of the remaining particles show the displacements toward the location of the annihilated particle, and its magnitude is larger for particles closer to its location. It is worth noting that the particles located at more than 860 nm from the heated position (the dotted open circle) show significant displacements. The magnon current does not affect these particles, which means that the driving force acting on these particles is the interaction. Figure 3c shows a cartoon of particle behaviors in the presence of a repulsive interparticle interaction before (top row) and after (bottom row) the annihilation of the rightest particle, consistent with the observed behavior. These results can also explain the L-TEM image of Figure 1d, where the distance (d) between the centers of skyrmions and antiskyrmions is almost retained at d ~335 nm. Besides, the fact that most of the remaining particles show displacement towards the location of the

annihilated particle regardless of their particle types suggests that the interparticle interaction is isotropic. We have also observed similar behaviors in the case of CW skyrmions (SI Figure S4). It summarizes all the observed behaviors as that the interaction is probably isotropic long-range repulsive one independent of the shapes and the skyrmion helicities.

While the inevitable presence of NT-bubbles and random distribution of skyrmions and antiskyrmions in the experiments hamper clear identification of the interaction, our micromagnetic simulations support the interpretation of the experimental results. We used a simulation model with two particles of a ACW (CW) skyrmion and an antiskyrmion aligned in the [100] and [110] directions. These arrangements investigated here cover every possibility considering shape and skyrmion helicities (SI Figure S5). To ensure that the simulations under periodic boundary conditions do not affect the two particles, we determined the sample size to be 2560×2560×100 nm^3 (SI Figure S6). Figure 3d shows energy as a function of the skyrmion-antiskyrmion distance of d at B_{c1}/B_0 where B_{c1} is the magnetic field where the skyrmion and antiskyrmion have the same energy, and B_0 is the normalization constant of magnetic fields. We find that the energy of every two-particle model increases and decreases as the skyrmion and the antiskyrmion approach and move apart from each other, respectively. Figure 3e shows conservative force converted from energy according to a previous study,[26] where the positive and negative values indicate repulsive and attractive. Every two-particle model always shows repulsive force, independent of relative position and skyrmion helicities. The repulsive force increases with decreasing d, while approaches asymptotically to zero far enough away at least d = 500 nm as shown in the inset of Figure 3e that is an enlarged view with differentiation. These features are consistent with the interpretation of the experimental results. Besides, the experiment and simulation results show that the interaction of skyrmion-skyrmion and antiskyrmion-

antiskyrmion is also isotropic long-range repulsive (SI Figure S7). The former is consistent with circular skyrmions showing a long-range repulsive interparticle interaction within the background ferromagnetic (FM) state in a *B*20-type chiral magnet.[26] Our result is a stark contrast to relative-position- and helicity-dependent short-range pairwise interactions between skyrmions and antiskyrmions simulated by 2D models for various magnetic systems,[3,19,20,23,32,33] and others,[34-38] and point out that short-range pairwise interaction is not universal. A recent computational study shows a stark difference in the trajectory of current-driven motion between skyrmions and antiskyrmions, resulting in a nonlinear regime and a complete breakdown of the single-particle picture.[25] Therefore, the nonlinear dynamic properties in the presence of repulsively interacting skyrmions and antiskyrmions may lead to the development of new spintronics devices for neuromorphic computing operating at the edge of chaos.[39,40]

In addition to the displacement, we found the deformation of elliptical skyrmions and square-shaped antiskyrmions depending on *d*. A representative example is shown in Figure 3f,g where we took the L-TEM images of a CW skyrmion and an antiskyrmion before and after annihilating a single spin texture with d ~460 nm and d ~360 nm, respectively, at a region of the sample with less bending. The elliptical skyrmion shows a subtle length change of the long axis (also see Figure 3h), while the antiskyrmion shows shape distortion (also see Figure 3i). Micromagnetic simulations support these experimental results. Figure 3j displays magnetization distribution maps, which show the change in the size and shape of the skyrmion and antiskyrmion depending on *d*.

Interestingly, our simulations show that the deformation of topological particles (skyrmions and antiskyrmions) exerts a significant influence on the change of the demagnetizing (E_d) and Zeeman energy (E_z) and the energy landscape. Here we compare the deformable to undeformable

topological particles and show a pair of the ACW skyrmion and antiskyrmion aligned along the [100] direction as a representative example. Figure 4a,b are the undeformable and deformable cases, respectively, which show the change of the magnetic energies from the reference distance of d = 1280 nm for the system with decreasing d. In the simulations for the undeformable case, we magnetically relaxed the system at each distance while fixing only the skyrmion and antiskyrmion structures identical with their isolated states of d = 1280 nm. The deformation brings a large increase in the E_d, whereas a large decrease in the E_z (Figure 4b), by comparison with the undeformable case (Figure 4a). In addition, the energy landscape in the deformable case is quite distinct from that in the undeformable case. With decreasing d, the undeformable topological particles show a negligible change in energy, while the background FM shows an increase (Figure 4c). On the other hand, the deformed skyrmion shows a significant increase in energy with decreasing d (Figure 4d) mainly due to the E_z and uniaxial anisotropy energy (SI Figure S8), indicating that the deformed skyrmion becomes energetically unstable. The FM shows a small decrease in energy. The deformed antiskyrmion shows a slight increase and then decrease. It is to be noted that, in the other arrangements and pairs, one or both of the two deformed topological particles show a significant increase in energy (SI Figure S9-S19). Many theoretical and experimental studies have shown the deformations of skyrmions so far, such as in motion by spin torque,[25,41-43] in a skyrmion structural transition,[44,45] and caused by external and internal fields.[46-54] Therefore, our findings that the deformation of the topological particles exerts a significant influence on the magnetic energies and energy landscape could also provide new insights into other properties associated with the deformation.[25,41-54]

In terms of topological stability, it seems odd that the topological particles would deform despite being energetically unstable. Therefore, we have investigated the individual magnetic

energy behaviors and found that the E_d of the deformed topological particles has a common feature without any exception in all arrangements and pairs (in 10 different combinations). Figure 4e,f show the E_d of the skyrmion and antiskyrmion with decreasing d, respectively. The orange and purple lines indicate the undeformable and deformable cases, respectively. The undeformable skyrmion and antiskyrmion show little change, whereas the deformable ones show a drop in the E_d with decreasing d, remarkably below d ~500 nm. The E_d reduction may be intrinsic to inhibit destabilizing the topological spin structures. The only exception is a pair of the antiskyrmions aligned along the [100] direction, where the magnetic energy behaviors are different from the other, except the E_d reduction and deformation of the antiskyrmions. This difference may originate from the unique magnetic structure of antiskyrmions, which connect smoothly with the demagnetizing fields coming from other antiskyrmions, confirmed by L-TEM (SI Figure S20). The total energy in the system for the deformable case is higher than that for the undeformable case (Figure 4g) in some cases, implying that the E_d reduction of the skyrmion and antiskyrmion is the first and foremost priority. Consequently, the deformation contributes to the repulsive force (Figure 4h).

Conclusion

In summary, we have unveiled a new type of skyrmion-antiskyrmion interaction in the Heusler material and the influences and cause of deformed skyrmions and antiskyrmions. Our study may provide new insights into the unresolved properties resulting from interacting skyrmions and antiskyrmions in condensed matter and other properties of deformed skyrmions in chiral magnets and multilayers.[25,41-54] Further, our results may conduce to opening a new subject as the

nonlinear current response properties[25] in the presence of repulsively interacting skyrmions and antiskyrmions and may offer a guide for developing skyrmion-antiskyrmion-based spintronic devices.[39,40]

Methods

We used a GPU-accelerated micromagnetic simulation program, MuMax[3],[55] where we programed anisotropic DMI and performed the simulations using a micromagnetic model by the ferromagnetic (FM) exchange, uniaxial anisotropy, anisotropic DMI,[3,8,11-13] Zeeman, and demagnetizing energies, with a size of 2560×2560×100 nm^3 on a 512×512×20 mesh under periodic boundary conditions for the x-y planes. We used an anisotropic DMI inherent in D_{2d} symmetry for the entire calculation area.[3,8,11-13] Magnetic structures were simulated by fully energy minimization using a conjugate gradient method. To calculate the demagnetizing field of the thin film, we used MuMax[3] build-in function "SetPBC(10,10,0)", that is, the demagnetizing field generated by 440 copies of the simulated area was taken into account.[55] The material parameters are the same as in ref. (11).

FIGURES

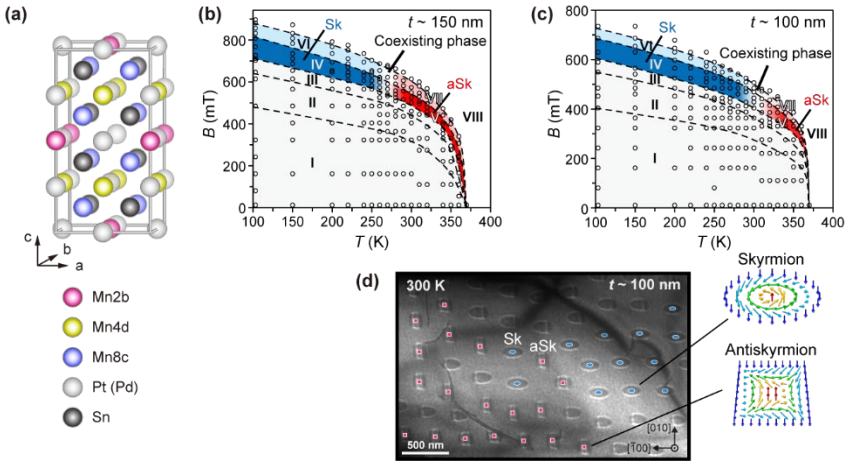

Figure 1. Phase diagrams and L-TEM image of a coexisting phase. (a) Crystal structure of Mn-Pt-Pd-Sn tetragonal inverse Heusler compounds. The colors represent the distinguished Wyckoff positions of space group *I*-42*m* in D_{2d} symmetry: magenta: Mn2b, yellow: Mn4d, blue: Mn8c, light gray: Pt (Pd), dark gray: Sn. (b),(c) Temperature-magnetic field phase diagrams for t ~150 nm (b) and t ~100 nm (c). The sample thickness has an error of ± 20 nm. Phases labeled with the (I)-(VIII) indicate helical (I), the coexistence of helical and NT-bubbles (II), NT-bubbles (III), skyrmions (IV), antiskyrmions (V), isolated skyrmions (VI), isolated antiskyrmions (VII), and ferromagnetism (VIII). The (I)-(III) phases were obtained at a constant tilt angle of $\theta = 15°$, while the (IV)-(VIII) phases at constant θ ~0°. Coexisting phases are in the temperature regions between the low-temperature skyrmion phase (IV and VI) and the high-temperature antiskyrmion phase (V and VII). Open circles in the phase diagrams are the points observed by L-TEM. In the phase diagrams (b),(c), temperature error arising from electron irradiation is about +10 K from the open circle points. (d) An L-TEM image of the room-temperature coexisting phase at 400 mT and t ~100 nm. We stamped skyrmions (Sk) and antiskyrmions (aSk) by the blue ellipses and red squares, respectively, and unstamped NT bubbles.

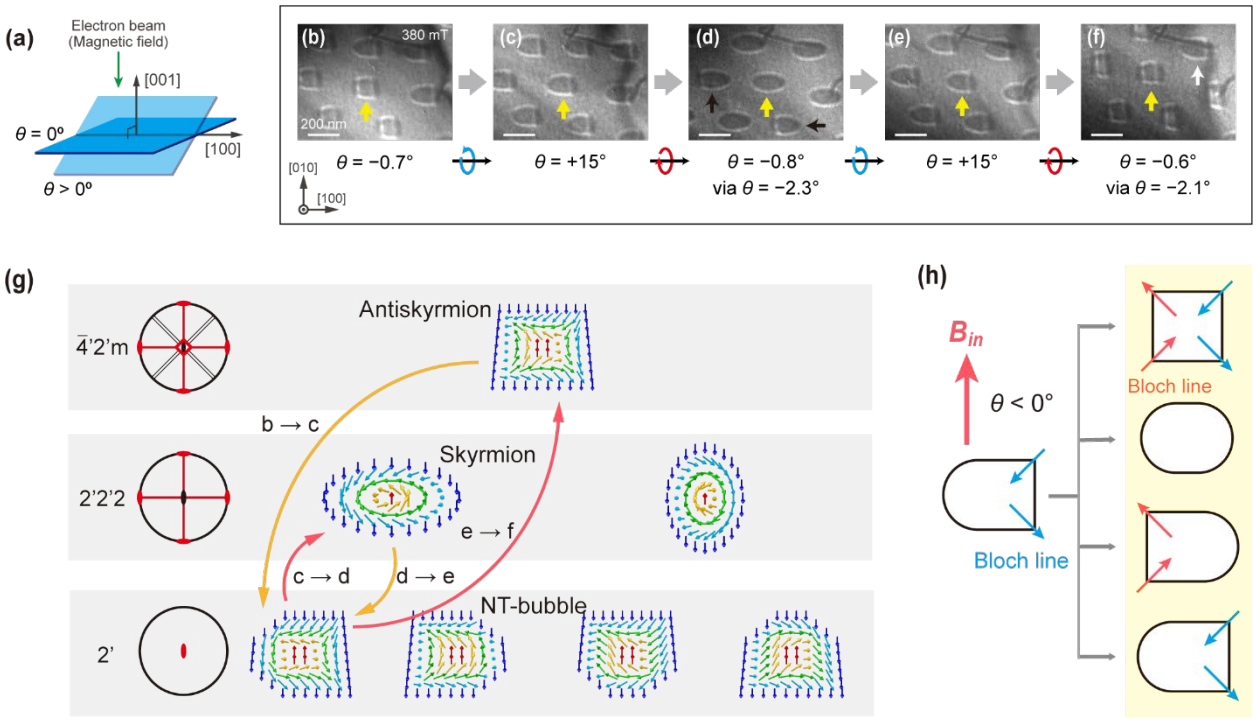

Figure 2. Stochastic reversible topological transformations between elliptical skyrmions and square-shaped antiskyrmions via NT-bubbles. (a) Schematic illustration of the sample tilt. We define the tilt angle as $\theta = 0°$ when the incident electron beam is parallel to the [001] direction describe the angle as θ when tilted with the [100] or [010] direction as the rotation axis. In our sample, the rotation axes in the [100] and [010] directions were to form the ACW and CW skyrmions, respectively. (b) L-TEM image at exactly $\theta = 0°$. The magnetic contrasts are obscure by a pitch-black contrast due to the diffraction contrast. (c)-(g) A series of under-focused L-TEM images of a stochastic reversible transformation between antiskyrmions and skyrmions. The rotation axis is in the [100] direction. We obtained these images by repeatedly tilting to $\theta = 15°$ and turning back to $\theta = \sim 0°$. The tilt angles when we obtained the L-TEM image are described below each image. The yellow arrows are distinct spin textures showing the antiskyrmion in (c),(g), skyrmion in (e), and NT-bubble in (d),(f). The black and white arrows represent the changed and unchanged NT-bubbles, respectively. (h) Three-dimensional magnetic point groups for antiskyrmions, skyrmions, and NT-bubbles in order of higher symmetry from the top. (i) Schematics of the mechanism of the stochastic transformations from the NT-bubble (the left) to the other spin structures (the right column) by the negative in-plane magnetic fields. The right column shows the antiskyrmion, skyrmion, changed NT-bubble, and unchanged NT-bubble, from top to bottom. The large red arrow represents the direction of negative in-plane magnetic fields (B_{in}). The small red and blue arrows represent Bloch lines of which the net magnetization component is parallel and antiparallel to B_{in}, respectively.

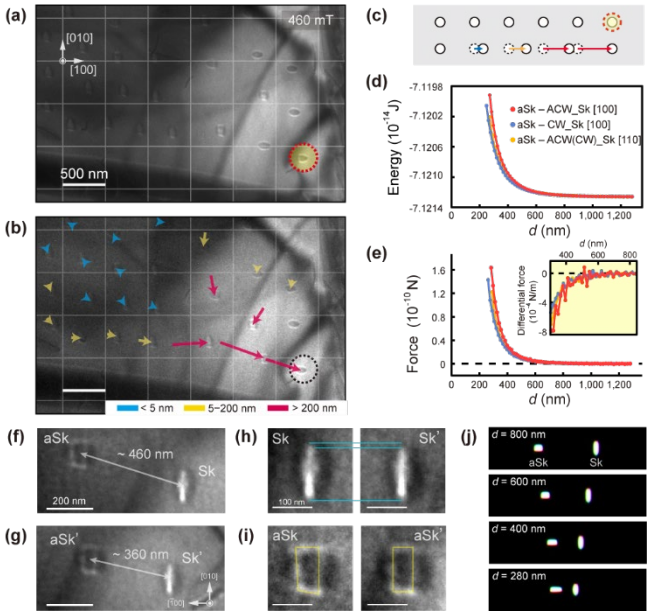

Figure 3. Particle displacements. (a),(b) Distributions of the particles (skyrmions, antiskyrmions, and NT-bubbles) before (a) and after (b) annihilating an NT-bubble by electron irradiation in 1.5 minutes. The red-dotted yellow (a) and black-dotted open (b) circles are the location before and after local heating. In (b), the color arrows indicate the direction and magnitude of the particle displacements from their initial positions in (a). The cells are eye guides for the scale 500 × 500 nm. (c) Schematic of particle displacements in a horizontal row with repulsion. Particles are at regular intervals before (upper) and after (lower) the annihilation of the rightmost particle. (d) Energy changes with decreasing d in the systems with the ACW (CW) skyrmion-antiskyrmion at B_{c1}/B_0. In the legends, "Sk" and "aSk" represent the skyrmion and antiskyrmion, and the numbers in parentheses represent the crystal orientations along which the two particles align. (e) Conservative force as the gradient of the energy in (d). Inset: A partial enlargement view that differentiates (e). (f),(g) L-TEM images of a CW skyrmion and an antiskyrmion at d ~460 nm (f) and ~360 nm (g) that were obtained before and after annihilating a single spin texture located outside of the images, respectively. (h),(i) Enlarged images of the skyrmion and antiskyrmion in (f),(g), respectively, The left and right sides display the images at d ~460 nm and ~360 nm, respectively. The blue and yellow lines are eye guides to appreciate small changes. (j) Magnetization distribution maps of the CW skyrmion and antiskyrmion for d = 800, 600, 400, and 280 nm from top to bottom.

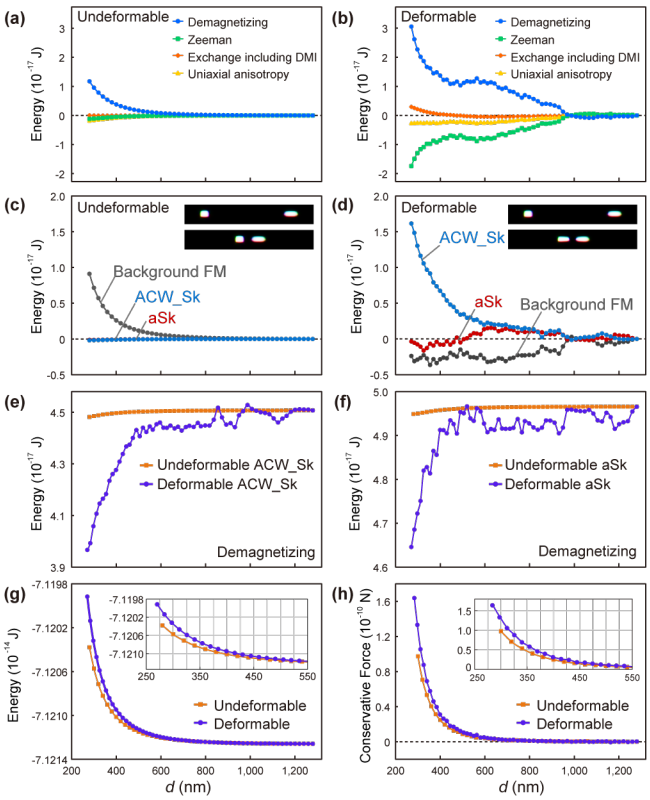

Figure 4. Simulated magnetic energy changes with decreasing d in the case where the antiskyrmion and ACW skyrmion are aligned along the [100] direction. We compare the deformable to undeformable cases. (a),(b) Changes of the demagnetizing (blue), Zeeman (green), exchange including DMI (orange), and uniaxial anisotropy (yellow) energies for the undeformable (a) and deformable (b) cases. (c),(d) Energy changes of the skyrmion (blue), antiskyrmion (red), and background FM (gray) for the undeformable (c) and deformable (d) cases. Figures (a),(b),(c),(d) display the energy change from $d = 1280$ nm. Insets: Magnetization distribution maps for $d = 1280$ nm (upper) and 280 nm (lower). (e),(f) Demagnetizing energy change of the skyrmion (e) and antiskyrmion (f). The orange and purple lines are the undeformable and deformable cases, respectively. (g),(h) Total energy (g) and conservative force (h). The colored lines are the same meanings in (e),(f). Insets: Enlarged views below $d = 550$ nm.

ASSOCIATED CONTENT

Structural characterization; Experimental and simulated helical spin structures; Annihilation of a spin texture by the local heating and the effect of magnon current; Displacement of particles in the case of CW skyrmions; List of all possible combinations of two topological particles; Normalized magnetic field of the coexistence of the skyrmion and antiskyrmion; Antiskyrmion-

antiskyrmion and skyrmion-skyrmion interactions; The other magnetic energy changes in aSk-ACW_Sk[100]; Deformation of topological particles; Magnetic energy changes in every combination other than aSk-ACW_Sk[100] and aSk-aSk[100]; Magnetic energy changes in aSk-aSk[100] and magnetic flux density map (PDF)

AUTHOR INFORMATION

Corresponding Author

Daigo Shimizu − Department of Electronics, Graduate School of Engineering, Nagoya University, 464-8603 Furocho, Chikusa-ku, Nagoya, Aichi, Japan; orcid.org/0000-0002-2981-5460; Email: shimizu.daigo.m1@s.mail.nagoya-u.ac.jp

Masahiro Nagao − Center for Integrated Research of Future Electronics, Institute of Materials and Systems for Sustainability, Nagoya University, 464-8601 Furocho, Chikusa-ku, Nagoya, Aichi, Japan; orcid.org/0000-0002-4956-1234; Email: nagao.masahiro@imass.nagoya-u.ac.jp

Author Contributions

D.S. and M.N. designed the experiment and wrote the manuscript. D.S. prepared the thin film, performed L-TEM experiments, micromagnetic simulations, EDX and EELS measurements, and analyzed the experimental data. T.N. performed micromagnetic simulations. Y.G.S. synthesized a bulk polycrystalline sample and preferred XRD measurements. M.K. and N.I. discussed the data and commented on the manuscript. M.N. supervised the study.

ACKNOWLEDGMENTS

We thank M. Araidai, S. Harada, K. Ishikawa, and H. Cheong for helpful discussions, and A. Akama, K. Higuchi, Y. Yamamoto for technical support of the TEM experiments. This work was supported by Nanotechnology Platform Project, MEXT, Japan, the JSPS KAKENHI (grant numbers 18K04679, 17H02737, 20K20899, 21H01029, 21K04626, and 21H04637), the JST-Mirai Program, Japan (grant number JPMJMI18G2), the joint usage/research program of the Institute of Materials and Systems for Sustainability (IMaSS), Nagoya University, and Young Researcher Grant from Center for Integrated Research of Future Electronics, IMaSS, Nagoya University.

REFERENCES

(1) Yu, X. Z.; Onose, Y.; Kanazawa, N.; Park, J. H.; Han, J. H.; Matsui, Y.; Nagaosa, N.; Tokura, Y. Real-space observation of a two-dimensional skyrmion crystal. *Nature* **2010**, 465 (7300), 901-904.

(2) Nayak, A. K.; Kumar, V.; Ma, T.; Werner, P.; Pippel, E.; Sahoo, R.; Damay, F.; Rößler, U. K.; Felser, C.; Parkin, S. S. P. Magnetic antiskyrmions above room temperature in tetragonal Heusler materials. *Nature* **2017**, 548 (7669), 561–566.

(3) Koshibae, W.; Nagaosa, N. Theory of antiskyrmions in magnets. *Nat. Commun*. **2016**, 7, 10542.

(4) Mühlbauer, S.; Binz, B.; Jonietz, F.; Pfleiderer, C.; Rosch, A.; Neubauer, A.; Georgii, R.; Böni, P. Skyrmion Lattice in a Chiral Magnet. *Science* **2009**, 323 (5916), 915.

(5) Tokunaga, Y.; Yu, X. Z.; White, J. S.; Rønnow, H. M.; Morikawa, D.; Taguchi, Y.; Tokura, Y. A New Class of Chiral Materials Hosting Magnetic Skyrmions Beyond Room Temperature. *Nat. Commun.* **2015**, 6, 7638.

(6) Kézsmárki, I.; Bordács, S.; Milde, P.; Neuber, E.; Eng, L. M.; White, J. S.; Rønnow, H. M.; Dewhurst, C. D.; Mochizuki, M.; Yanai, K.; Nakamura, H.; Ehlers, D.; Tsurkan, V.; Loidl, A. Néel-type skyrmion lattice with confined orientation in the polar magnetic semiconductor GaV_4S_8. *Nat. Mater.* **2015**, 14, 1116– 1122.

(7) Jiang, W.; Upadhyaya, P.; Zhang, W.; Yu, G.; Jungfleisch, M. B.; Fradin, F. Y.; Pearson, J. E.; Tserkovnyak, Y.; Wang, K. L.; Heinonen, O.; Te Velthuis, S. G. E.; Hoffmann, A. Blowing Magnetic Skyrmion Bubbles. *Science* **2015**, 349 (6245), 283– 286.

(8) Saha, R.; Srivastava, A. K.; Ma, T.; Jena, J.; Werner, P.; Kumar, V.; Felser, C.; Parkin, S. S. P. Intrinsic stability of magnetic anti-skyrmions in the tetragonal inverse Heusler compound $Mn_{1.4}Pt_{0.9}Pd_{0.1}Sn$. *Nat. Commun*. **2019**, 10, 5305.

(9) Jamaluddin, S.; Manna, S. K.; Giri, B.; Madduri, P. V. P.; Parkin, S. S. P.; Nayak, A. K. Robust Antiskyrmion Phase in Bulk Tetragonal Mn–Pt(Pd)–Sn Heusler System Probed by Magnetic Entropy Change and AC-Susceptibility Measurements. *Adv. Funct. Mater*. **2019**, 29 (24), 1901776.

(10) Vir, P.; Gayles, J.; Sukhanov, A. S.; Kumar, N.; Damay, F.; Sun, Y.; Kübler, J.; Shekhar, C.; Felser, C. Anisotropic topological Hall effect with real and momentum space Berry curvature in the antiskrymion-hosting Heusler compound $Mn_{1.4}PtSn$. *Phys. Rev. B* **2019**, 99 (14), 140406(R).

(11) Peng, L.; Takagi, R.; Koshibae, W.; Shibata, K.; Nakajima, K.; Arima, T.; Nagaosa, N.; Seki, S.; Yu, X. Z.; Tokura, Y. Controlled transformation of skyrmions and antiskyrmions in a non-centrosymmetric magnet. *Nat. Nanotechnol*. **2020**, 15 (3), 181–186.

(12) Jena, J.; Göbel, B.; Ma, T.; Kumar, V.; Saha, R.; Mertig, I.; Felser, C.; Parkin, S. S. P. Elliptical Bloch skyrmion chiral twins in an antiskyrmion system. *Nat. Commun*. **2020**, 11 (1), 1115.

(13) Jena, J.; Göbel, B.; Kumar, V.; Mertig, I.; Felser, C.; Parkin, S. Evolution and competition between chiral spin textures in nanostripes with D_{2d} symmetry. *Sci. Adv*. **2020**, 6 (49), eabc0723.

(14) Kumar, V.; Kumar, N.; Reehuis, M.; Gayles, J.; Sukhanov, A. S.; Hoser, A.; Damay, F.; Shekhar, C.; Adler, P.; Felser, C. Detection of antiskyrmions by topological Hall effect in Heusler compounds. *Phys. Rev. B* **2020**, 101 (1), 014424.

(15) Madduri, P. V. P.; Sen, S.; Giri, B.; Chakrabartty, D.; Manna, S. K.; Parkin, S. S. P.; Nayak, A. K. ac susceptibility study of magnetic relaxation phenomena in the antiskyrmion-hosting tetragonal Mn-Pt(Pd)-Sn system. *Phys. Rev. B* **2020**, 102 (17), 174402.

(16) Ma, T.; Sharma, A. K.; Saha, R.; Srivastava, A. K.; Werner, P.; Vir, P.; Kumar, V.; Felser, C.; Parkin, S. S. P. Tunable Magnetic Antiskyrmion Size and Helical Period from Nanometers to Micrometers in a D_{2d} Heusler Compound. *Adv. Mater*. **2020**, 32 (28), 2002043.

(17) Cespedes, B. E. Z.; Vir, P.; Milde, P.; Felser, C.; Eng, L. M. Critical sample aspect ratio and magnetic field dependence for antiskyrmion formation in $Mn_{1.4}PtSn$ single crystals. *Phys. Rev. B* **2021**, 103 (18), 184411.

(18) Karube, K.; Peng, L.; Masell, J.; Yu, X. Z.; Kagawa, F.; Tokura, Y.; Taguchi, Y. Room-temperature antiskyrmions and sawtooth surface textures in a non-centrosymmetric magnet with S_4 symmetry. *Nat. Mater*. **2021**, 20 (3), 335–340.

(19) Lin, S.-Z.; Hayami, S. Ginzburg-Landau theory for skyrmions in inversion-symmetric magnets with competing interactions. *Phys. Rev. B* **2016**, 93 (6), 064430.

(20) Leonov, A. O.; Mostovoy, M. Multiply periodic states and isolated skyrmions in an anisotropic frustrated magnet. *Nat. Commun*. **2015**, 6, 8275.

(21) Hu, Y.; Chi, X.; Li, X.; Liu, Y.; Du, A. Creation and Annihilation of Skyrmions in the Frustrated Magnets with Competing Exchange Interactions. *Sci. Rep*. **2017**, 7, 16079.

(22) Okubo, T.; Chung, S.; Kawamura, H. Multiple-*q* States and the Skyrmion Lattice of the Triangular-Lattice Heisenberg Antiferromagnet under Magnetic Fields. *Phys. Rev. Lett*. **2012**, 108 (1), 017206.

(23) Zhang, X.; Xia, J.; Zhou, Y.; Liu, X.; Zhang, H.; Ezawa, M. Skyrmion dynamics in a frustrated ferromagnetic film and current-induced helicity locking-unlocking transition. *Nat. Commun*. **2017**, 8, 1717.

(24) Leonov, A. O.; Mostovoy, M. Edge states and skyrmion dynamics in nanostripes of frustrated magnets. *Nat. Commun*. **2017**, 8, 14394.

(25) Ritzmann, U.; von Malottki, S.; Kim, J.-V.; Heinze, S.; Sinova, J.; Dupé, B. Trochoidal motion and pair generation in skyrmion and antiskyrmion dynamics under spin–orbit torques. *Nat. Electron*. **2018**, 1 (8), 451-457.

(26) Hoffmann, M,; Müller, G. P.; Melcher, C.; Blügel, S.; Skyrmion-Antiskyrmion Racetrack Memory in Rank-One DMI Materials. *Front. Phys.* **2021**, 9, 769873.

(27) Du, H.; Zhao, X.; Rybakov, F. N.; Borisov, A. B.; Wang, S.; Tang, J.; Jin, C.; Wang, C.; Wei, W.; Kiselev, N. S.; Zhang, Y.; Che, R.; Blügel, S.; Tian, M. Interaction of Individual Skyrmions in a Nanostructured Cubic Chiral Magnet. *Phys. Rev. Lett*. **2018**, 120 (19), 197203.

(28) Lin, S.-Z.; Reichhardt, C.; Batista, C. D.; Saxena, A. Particle model for skyrmions in metallic chiral magnets: Dynamics, pinning, and creep. *Phys. Rev. B* **2013**, 87 (21), 214419.

(29) Shibata, K.; Yu, X. Z.; Hara, T.; Morikawa, D.; Kanazawa, N.; Kimoto, K.; Ishiwata, S.; Matsui, Y.; Tokura, Y. Towards control of the size and helicity of skyrmions in helimagnetic alloys by spin–orbit coupling. *Nat. Nanotechnol*. **2013**, 8 (10), 723–728.

(30) Camosi, L.; Rougemaille, N.; Fruchart, O.; Vogel, J.; Rohart, S.; Micromagnetics of antiskyrmions in ultrathin films. *Phys. Rev. B* **2018**, 97, 134404.

(31) Koshibae, W.; Nagaosa, N. Creation of skyrmions and antiskyrmions by local heating. *Nat. Commun*. **2014**, 5, 5148.

(32) Kuchkin, V. M.; Kiselev, N. S. Turning a chiral skyrmion inside out. *Phys. Rev. B* **2020**, 101 (6), 064408.

(33) Everschor-Sitte, K.; Sitte, M.; Valet, T.; Abanov, A.; Sinova, J. Skyrmion production on demand by homogeneous DC currents. *New J. Phys*. **2017**, 19, 092001.

(34) Price, H. M.; Cooper, N. R. Skyrmion-antiskyrmion pairs in ultracold atomic gases. *Phys. Rev. A* **2011**, 83 (6), 061605(R).

(35) Cooper, N. R. Solitary Waves of Planar Ferromagnets and the Breakdown of the Spin-Polarized Quantum Hall Effect. *Phys. Rev. Lett*. **1998**, 80 (20), 4554–4557.

(36) Luo, W.; Côté, R. Zeeman coupling and screening corrections to skyrmion excitations in graphene. *Phys. Rev. B* **2013**, 88 (11), 115417.

(37) Luo, W.; Côté, R. Transport gap and hysteretic behavior of the Ising quantum Hall ferromagnets in |N|>0 Landau levels of bilayer graphene. *Phys. Rev. B* **2014**, 90 (24), 245410.

(38) Wu, F.; Sarma, S. D. Collective Excitations of Quantum Anomalous Hall Ferromagnets in Twisted Bilayer Graphene. *Phys. Rev. Lett*. **2020**, 124 (4), 046403.

(39) Bertschinger, N.; Natschläger, T. Real-Time Computation at the Edge of Chaos in Recurrent Neural Networks. *Neural Comput*. **2004**, 16 (7), 1413–1436.

(40) Grollier, J.; Querlioz, D.; Camsari, K. Y.; Everschor-Sitte, K.; Fukami, S.; Stiles, M. D.; Neuromorphic spintronics. *Nat. Electron*. **2020**, 3 (7), 360–370.

(41) Lin, S.-Z. Reichhardt, C.; Batista, C. D.; Saxena, A. Driven Skyrmions and Dynamical Transitions in Chiral Magnets. *Phys. Rev. Lett*. **2013**, 110 (20), 207202.

(42) Masell, J.; Rodrigues, D. R.; McKeever, B. F.; Everschor-Sitte, K. Spin-transfer torque driven motion, deformation, and instabilities of magnetic skyrmions at high currents. *Phys. Rev. B* **2020**, 101 (21), 214428.

(43) Litzius, K.; Leliaert, J.; Bassirian, P.; Rodrigues, D.; Kromin, S.; Lemesh, I.; Zazvorka, J.; Lee, K.-J.; Mulkers, J.; Kerber, N.; Heinze, D.; Keil, N.; Reeve, R. M.; Weigand, M.; Van Waeyenberge, B.; Schütz, G.; Everschor-Sitte, K.; Beach, G. S. D.; Kläui, M. The role of temperature and drive current in skyrmion dynamics. *Nat. Electron*. **2020**, 3 (1), 30–36.

(44) Morikawa, D.; Yu, X.; Karube, K.; Tokunaga, Y.; Taguchi, Y.; Arima, T.; Tokura, Y. Deformation of Topologically-Protected Supercooled Skyrmions in a Thin Plate of Chiral Magnet $Co_8Zn_8Mn_4$. *Nano Lett*. **2017**, 17 (3), 1637–1641.

(45) Takagi, R.; Yamasaki, Y.; Yokouchi, T.; Ukleev, V.; Yokoyama, Y.; Nakao, H.; Arima, T.; Tokura, Y.; Seki, S. Particle-size dependent structural transformation of skyrmion lattice. *Nat. Commun*. **2020**, 11 (1), 5685.

(46) Wilson, M. N.; Karhu, E. A.; Quigley, A. S.; Rößler, U. K.; Butenko, A. B.; Bogdanov, A. N.; Robertson, M. D.; Monchesky, T. L. Extended elliptic skyrmion gratings in epitaxial MnSi thin films. *Phys. Rev. B* **2012**, 86 (14), 144420.

(47) White, J. S.; Prša, K.; Huang, P.; Omrani, A. A.; Živković, I.; Bartkowiak, M.; Berger, H.; Magrez, A.; Gavilano, J. L.; Nagy, G.; Zang, J.; Rønnow, H. M. Electric-Field-Induced Skyrmion Distortion and Giant Lattice Rotation in the Magnetoelectric Insulator Cu_2OSeO_3. *Phys. Rev. Lett.* **2014**, 113 (10), 107203.

(48) Shibata, K.; Iwasaki, J.; Kanazawa, N.; Aizawa, S.; Tanigaki, T.; Shirai, M.; Nakajima, T.; Kubota, M.; Kawasaki, M.; Park H. S.; Shindo, D.; Nagaosa, N.; Tokura, Y. Large anisotropic deformation of skyrmions in strained crystal. *Nat. Nanotechnol*. **2015**, 10 (7), 589–592.

(49) Ukleev, V.; Yamasaki, Y.; Morikawa, D.; Karube, K.; Shibata, K.; Tokunaga, Y.; Okamura, Y.; Amemiya, K.; Valvidares, M.; Nakao, H.; Taguchi, Y.; Tokura, Y.; Arima, T. Element-specific soft x-ray spectroscopy, scattering, and imaging studies of the skyrmion-hosting compound $Co_8Zn_8Mn_4$. *Phys. Rev. B* **2019**, 99 (14), 144408.

(50) Nagase, T.; Komatsu, M.; So, Y. G.; Ishida, T.; Yoshida, H.; Kawaguchi, Y.; Tanaka, Y.; Saitoh, K.; Ikarashi, N.; Kuwahara, M.; Nagao, M. Smectic Liquid-Crystalline Structure of Skyrmions in Chiral Magnet $Co_{8.5}Zn_{7.5}Mn_4$(110) Thin Film. *Phys. Rev. Lett*. **2019**, 123 (13), 137203.

(51) El Hog, S.; Kato, F.; Koibuchi, H.; Diep, H. T. Finsler geometry modeling and Monte Carlo study of skyrmion shape deformation by uniaxial stress. *Phys. Rev. B* **2021**, 104 (2), 024402.

(52) Kameda, M.; Koyama, R.; Nakajima, T.; Kawaguchi, Y. Controllable interskyrmion attractive interactions and resulting skyrmion-lattice structures in two-dimensional chiral magnets with in-plane anisotropy. *Phys. Rev. B* **2021**, 104 (17), 174446.

(53) Aqeel, A.; Sahliger, J.; Taniguchi, T.; Mändl, S.; Mettus, D.; Berger, H.; Bauer, A.; Garst, M.; Pfleiderer, C.; Back, C. H. Microwave Spectroscopy of the Low-Temperature Skyrmion State in Cu_2OSeO_3. *Phys. Rev. Lett*. **2021**, 126 (1), 017202.

(54) Ba, Y.; Zhuang, S.; Zhang, Y.; Wang, Y.; Gao, Y.; Zhou, H.; Chen, M.; Sun, W.; Liu, Q.; Chai, G.; Ma, J.; Zhang, Y.; Tian, H.; Du, H.; Jiang, W.; Nan, C.; Hu, J.-M.; Zhao, Y. Electric-field control of skyrmions in multiferroic heterostructure via magnetoelectric coupling. *Nat. Commun*. **2021**, 12 (1), 322.

(55) Vansteenkiste, A.; Leliaert, J.; Dvornik, M.; Helsen, M.; Garcia-Sanchez, F.; Van Waeyenberge, B. The design and verification of MuMax3. *AIP Adv*. **2014**, 4 (10), 107133.

Supporting Information

Nanoscale characteristics of a room-temperature coexisting phase of magnetic skyrmions and antiskyrmions for skyrmion-antiskyrmion-based spintronic applications

Daigo Shimizu,[1]* Tomoki Nagase,[1] Yeong-Gi So,[2] Makoto Kuwahara,[3] Nobuyuki Ikarashi,[1,4] and Masahiro Nagao[1,4†]

[1] *Department of Electronics, Nagoya University, Nagoya, Japan*

[2] *Department of Materials Science, Akita University, Akita, Japan*

[3] *Advanced Measurement Technology Center, Institute of Materials and Systems for Sustainability, Nagoya University, Nagoya, Japan*

[4] *Center for Integrated Research of Future Electronics, Institute of Materials and Systems for Sustainability, Nagoya University, Nagoya, Japan*

*To whom correspondence should be addressed.

shimizu.daigo.m1@s.mail.nagoya-u.ac.jp

†To whom correspondence should be addressed.

nagao.masahiro@imass.nagoya-u.ac.jp

CONTENTS

I: Structural characterization

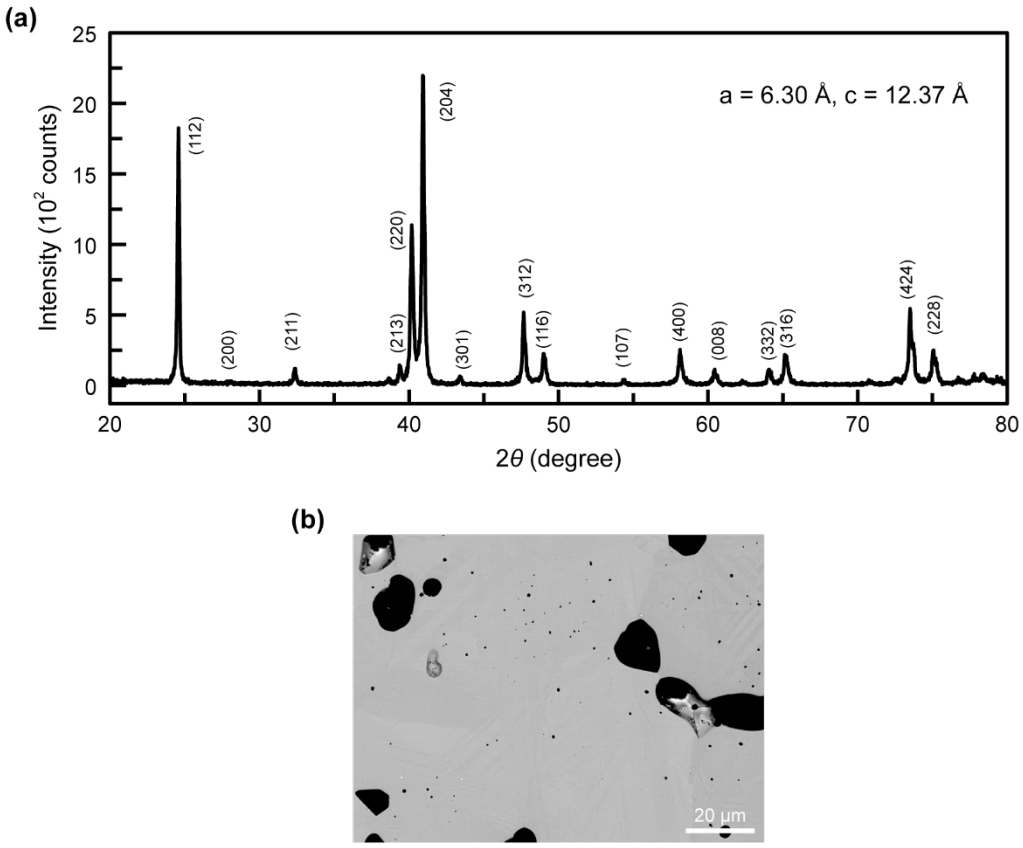

Figure S1. Structural characterization at room temperature. (a) Powder X-ray diffraction (XRD) profile at room temperature for $Mn_{1.3}Pt_{1.0}Pd_{0.1}Sn$. (b) FE-SEM image of bulk sample surface of

$Mn_{1.3}Pt_{1.0}Pd_{0.1}Sn$.

Mn	Pt	Pd	Sn
1.30(1)	0.98(2)	0.09(1)	1.00(2)

Table S1. Chemical composition in the observed region determined by energy dispersive x-ray spectroscopy (EDS).

II: Experimental and simulated helical spin structures

We observe the coexisting phase at room-temperature in $Mn_{1.3}Pt_{1.0}Pd_{0.1}Sn$ with $t \sim 100$ nm (Figure 1(c)(d)), while the previous studies reported the coexisting one at $T_{CO} = 268$ K in $Mn_{1.4}Pt_{0.9}Pd_{0.1}Sn$ with $t \sim 100$ nm. This difference is due to the difference in the magnitude of the isotropic DMI constant (D) because, as the D decreases, the higher-temperature antiskyrmion phase becomes unstable and the lower-temperature skyrmion phase becomes relatively stable, increasing T_{CO} as evidenced by Figure 1(b),(c). At a zero magnetic field, the period (λ) of helical spin structure is proportional to A/D,[1] where A is the exchange stiffness constant proportional to a Curie temperature of T_C. The Curie temperatures of $Mn_{1.3}Pt_{1.0}Pd_{0.1}Sn$ and $Mn_{1.4}Pt_{0.9}Pd_{0.1}Sn$ are almost the same (Figure 1(b),(c) and ref. (2)). In other words, the difference in the λ reflects the difference in the D. Figure S2(a) shows an L-TEM image in our sample with $t \sim 100$ nm at a zero magnetic field. The helical period is $\lambda = 200 \pm 5$ nm that is shorter than $\lambda = 140 \pm 15$ nm in $Mn_{1.4}Pt_{0.9}Pd_{0.1}Sn$.[2] We, therefore, conclude that the D of our sample is smaller than that of $Mn_{1.4}Pt_{0.9}Pd_{0.1}Sn$.

We compare the helical period between the results of the L-TEM experiment (Figure S2(a)) and the micromagnetic simulation with $t = 100$ nm (Figure S2(b)). The material parameters are the same as in ref. (2). We also show a simulated L-TEM image (Figure S2(c)) based on the micromagnetic simulations (Figure S2(b)), to facilitate comparison with the experimental L-TEM image (Figure S2(a)). In Figure S2(b),(c), the simulated helical period is $\lambda = 196.9$ nm, which is in close agreement with $\lambda = 200 \pm 5$ nm confirmed by the experimental L-TEM result (Figure S2(a)].

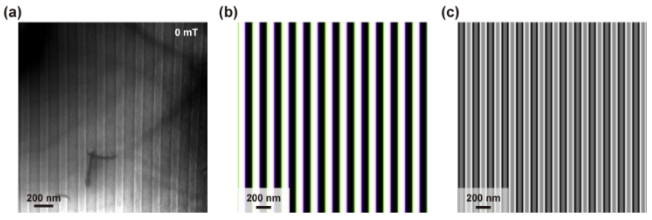

Figure S2. Experimental and simulated helical spin structures at a zero magnetic field. (a) An experimental L-TEM image in $Mn_{1.3}Pt_{1.0}Pd_{0.1}Sn$ with $t \sim 100$ nm. The helical period is $\lambda = 200 \pm 5$ nm. The dark line contrasts paralleled not to the stripe contrasts are the bend contours where Bragg condition is locally satisfied due to sample bend. The dogleg pitch-black line contrast around the lower middle is due to the sample defects. (b) Simulated stable magnetic structure using micromagnetic simulations with $t =$ 100 nm. The black and white colors represent downward and upward perpendicular magnetization, respectively. (c) Simulated L-TEM image based on (b). The simulated helical period is $\lambda = 196.9$ nm in (b),(c).

III : Annihilation of a spin texture by the local heating and the effect of magnon current

We confirmed the annihilation of a single antiskyrmion. A theory has proposed that local heating enables annihilating a single spin texture.[3] In this study, we have used a focused electron beam to apply local heating (Figure S3(a)). Figure S3(b),(c) show L-TEM images before and after the annihilation of the single antiskyrmion, respectively. In Figure S2(b), the single antiskyrmion exists. We have exposed the single antiskyrmion to the focused electron beam with a diameter of ~200 nm at the yellow-shaded circle in Figure S3(b). We confirm that the antiskyrmion annihilates after electron irradiation in 2 minutes, as shown in Figure S3(c).

Although demonstrating the annihilation of the single antiskyrmion by local heating, we cannot ignore the effect of the thermal current (magnon current) caused by local heating on the spin structure. Magnon current exerts on the drive of skyrmions and antiskyrmions.[4-7] Our purpose is to observe the displacement of skyrmions and antiskyrmions only driven by the skyrmion-antiskyrmion interactions. Therefore, it is necessary to determine the range of distances from the local heating position that magnon current does not exert on the drive of skyrmions and antiskyrmions. In Figure S3(d), an electron beam with $r \sim 200$ nm was focused at a distance of ~700 nm away from the antiskyrmion. After local electron irradiation in 2 minutes, although the antiskyrmion slightly shifted away from the local heating position (Figure S3(e)), the magnon current is insufficient to drive the antiskyrmion under this experimental condition where the heat current density decays in inverse proportion to distance. In other words, magnon current does not affect skyrmions and antiskyrmions at a distance of more than at least 700 nm from the local heating position.

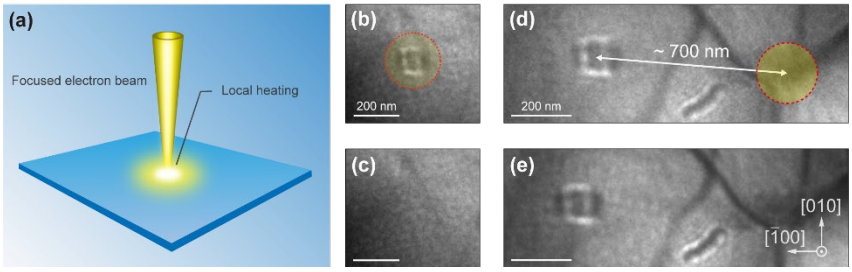

Figure S3. Demonstration of the annihilation of a single antiskyrmion by a focused electron beam and the examination of the effect of the thermal (magnon) current on an antiskyrmion. (a) Schematic of local heating with the focused electron beam. (b),(c) Experimental demonstration of the annihilation of the antiskyrmion by local heating. The L-TEM images show the states before and after local electron irradiation with a diameter of $r \sim 200$ nm (yellow-shaded circle) in 2 minutes, respectively. (d),(e) The examination of thermal (magnon) current effect on the antiskyrmion. The L-TEM images show the states before and after local electron irradiation ($r \sim 200$ nm, yellow-shaded circle) in 2 minutes. The worm-like contrast in the middle is a defect on the sample.

IV : Displacement of particles in the case of CW skyrmions

We have investigated the particle displacement in the presence of CW skyrmions in the same way as ACW skyrmions (Figure 2(a),(b)). Figures S4(a),(b) show the particle distributions before and after local heating by the focused electron beam with r ~200 nm in 1.5 minutes, respectively. The particle displacement is similar to that in the presence of ACW skyrmions (Figure 2(a),(b)).

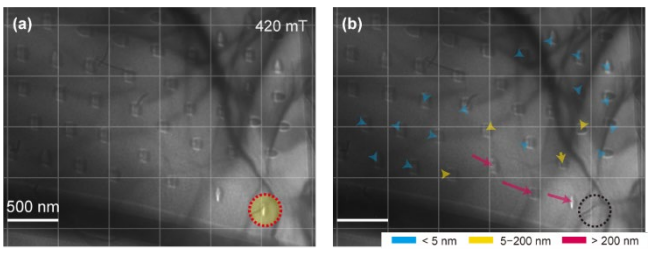

Figure S4. Particle displacements in the presence of CW skyrmions. (a),(b) Distributions of the particles (CW skyrmions, antiskyrmions, and NT-bubbles) before (a) and after (b) that a CW skyrmion was annihilated by electron irradiation with a diameter of r ~200 nm in 1.5 minutes. The red-dotted yellow (a) and black-dotted open (b) circles are the locations before and after local heating. In (b), the color arrows indicate the direction and magnitude of the particle displacements from their initial positions in (a). The cells are eye guides for the scale 500 × 500 nm.

V: List of all possible combinations of two topological particles

In this study, we have used micromagnetic simulations to investigate the magnetic energy in the presence of the two topological particles. All possible combinations are ten, listed in Table. S2. The same-colored characters (magenta, yellow, cyan) indicate equivalent arrangements. We have simulated every possible combination.

No.	Topological particle 1	Topological particle 2	Aligned crystal direction	Abbreviated notation
1	Antiskyrmion	Anticlockwise Skyrmion	[100]	aSk-ACW_Sk [100]
1	Antiskyrmion	Clockwise Skyrmion	[010]	aSk-CW_Sk [010]
2	Antiskyrmion	Anticlockwise Skyrmion	[110]	aSk-ACW_Sk [110]
2	Antiskyrmion	Clockwise Skyrmion	[110]	aSk-CW_Sk [110]
3	Antiskyrmion	Clockwise Skyrmion	[100]	aSk-CW_Sk [100]
3	Antiskyrmion	Anticlockwise Skyrmion	[010]	aSk-ACW_Sk [010]
4	Anticlockwise Skyrmion	Anticlockwise Skyrmion	[100]	ACW_Sk-ACW_Sk [100]
5	Anticlockwise Skyrmion	Anticlockwise Skyrmion	[110]	ACW_Sk-ACW_Sk [110]
6	Clockwise Skyrmion	Anticlockwise Skyrmion	[100]	CW_Sk-ACW_Sk [100]
7	Clockwise Skyrmion	Anticlockwise Skyrmion	[110]	CW_Sk-ACW_Sk [110]
8	Clockwise Skyrmion	Clockwise Skyrmion	[100]	CW_Sk-CW_Sk [100]
9	Antiskyrmion	Antiskyrmion	[110]	aSk-aSk [110]
10	Antiskyrmion	Antiskyrmion	[100]	aSk-aSk [100]

Table. S2. All possible combinations in the two-particle model. In the abbreviation notation, CW_Sk and ACW_Sk denote the clockwise and counterclockwise skyrmions, respectively. aSk denotes the antiskyrmion. The numbers in parentheses represent the crystal directions along which the two particles are arranged. The purple-, yellow-, and blue-colored characters correspond to Figure S5 (the same color is equivalent).

Figure S5 shows schematic arrangements of elliptical skyrmions with helicity degrees of freedom (CW and ACW) and square-shaped antiskyrmions. We have investigated the three skyrmion-antiskyrmion arrangements in the top row. Arrangements surrounded by the same color (magenta, yellow, cyan) indicate equivalent arrangements, indicating that all the skyrmion-antiskyrmion arrangements are covered only by the arrangements in the top row.

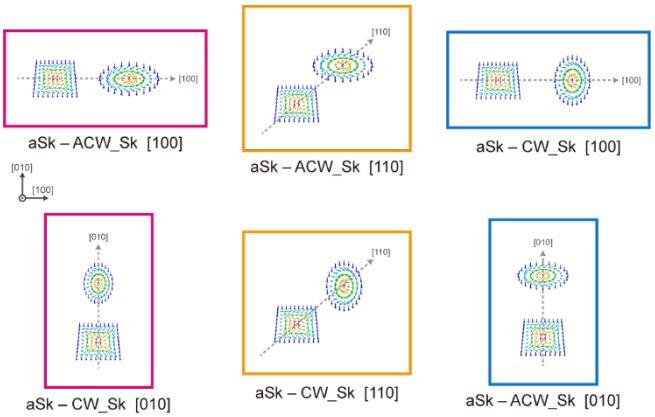

Figure S5. Schematic illustrations of arrangements of the two particles composed of elliptical skyrmions with helicity degrees of freedom (CW and ACW) and square-shaped antiskyrmions. Arrangements surrounded by the same color (magenta, yellow, cyan) indicate equivalent arrangements.

VI: Normalized magnetic field of the coexistence of the skyrmion and antiskyrmion

To perform micromagnetic simulation in the coexistence of skyrmions and antiskyrmions, we calculated a magnetic field of B_{c1}/B_0 at which the skyrmion and antiskyrmion have the same energy density. B_0, the normalization constant of a magnetic field, is defined as $B_0 = D^2/2M_{sat}A$. Figure S6 shows subtracted energy density ε_{sk} (blue) and ε_{ask} (red) as a function of the normalized magnetic field B/B_0. ε_{sk} and ε_{ask} represent the energy densities that subtract the ferromagnetic energy density from the skyrmion and antiskyrmion energy densities, respectively. We observe the intersection between the ε_{sk} and ε_{ask} lines at $B_{c1}/B_0 = 13.283$ at which point is that the skyrmion and antiskyrmion have the same energy density. In this study, therefore, we performed the simulations using $B_{c1}/B_0 = 13.283$.

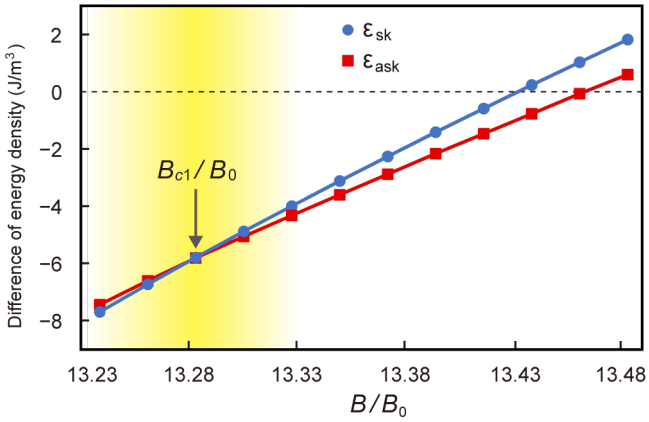

Figure S6. Normalized magnetic field B/B_0 dependence of subtracted energy density ε_{sk} (blue) and ε_{ask}

(red). ε_{sk} and ε_{ask} represent the energy densities that subtract the ferromagnetic energy density from the skyrmion and antiskyrmion energy densities, respectively. We define B_{c1}/B_0 as the point of the intersection between the ε_{sk} and ε_{ask} lines. The B_{c1}/B_0 is 13.283.

VII: Antiskyrmion-antiskyrmion and skyrmion-skyrmion interactions

Our micromagnetic simulations show that the skyrmion-skyrmion and antiskyrmion-antiskyrmion interactions are isotropic at B_{c1}/B_0, where the skyrmion and the antiskyrmion have the same energy density. Figures S7(a),(b) show energy density as a function of the skyrmion-skyrmion and antiskyrmion-antiskyrmion distances, respectively. We simulated the three and two arrangements for skyrmions and antiskyrmions, respectively, which covered every possibility considering the shape and skyrmion helicities. Every result show that energy density increases as the skyrmion-skyrmion and antiskyrmion-antiskyrmion distances decrease, indicating that the interactions are isotropic long-range repulsive interactions at the coexisting phase similar to the skyrmion-antiskyrmion interaction.

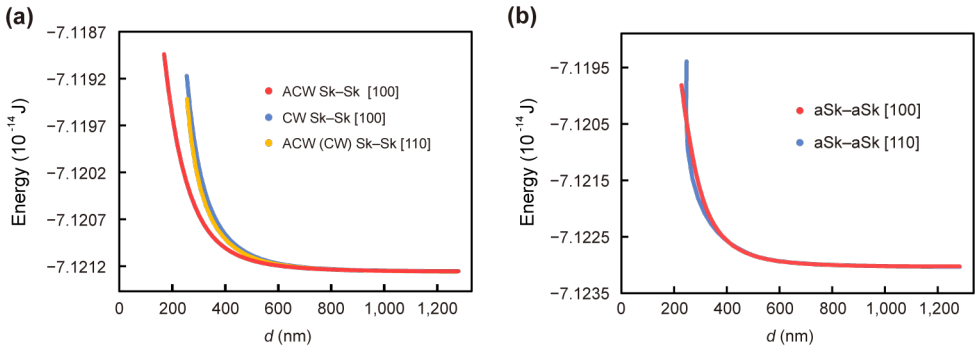

Figure S7. Antiskyrmion-antiskyrmion and skyrmion-skyrmion interactions. (a) Simulated energy density as a function of the ACW (CW) skyrmion-skyrmion distance aligned in the [100] ([100]) and [110] directions at B_{c1}/B_0, using two-particle models. (b) Antiskyrmion-antiskyrmion distance dependence of simulated energy density. The two antiskyrmions are aligned axially in the [100] and [110] directions at B_{c1}/B_0.

VIII: The other magnetic energy changes in aSk-ACW_Sk[100]

In Figure 4 in the main text, we show the magnetic energy changes with decreasing d in aSk-ACW_Sk[100] as a representative example. Figure S8 shows the other magnetic energy changes in

aSk-ACW_Sk[100]. The uniaxial anisotropy and Zeeman energies contribute to increasing the deformed ACW skyrmion energy (Figure S8(b)), indicating that the magnetization component in the ± z-direction (perpendicular to the plane) decreases with deformation.

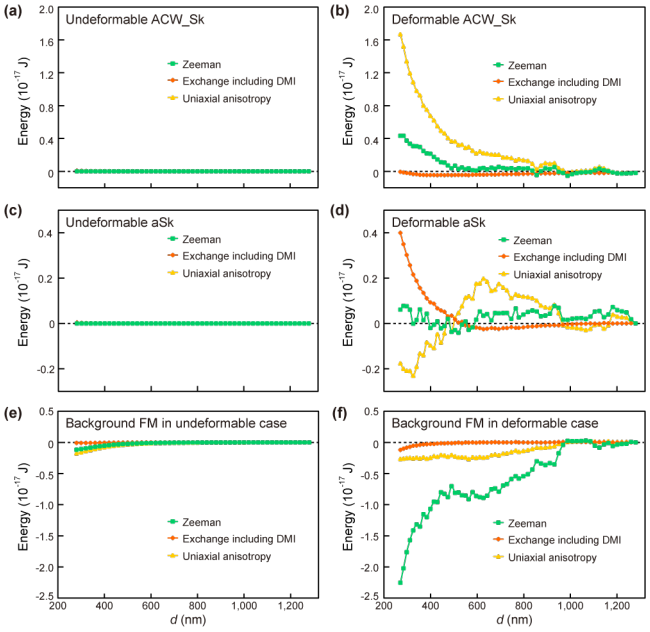

Figure S8. The other magnetic energy changes with decreasing d in aSk-ACW_Sk[100]. (a)-(f) Changes of the Zeeman (green), exchange including DMI (orange), and uniaxial anisotropy (yellow) energies for the undeformable (a) and deformable (b) ACW skyrmion, the undeformable (c) and deformable (d) antiskyrmion, and the background FM in the undeformable (e) and deformable (f) case.

IX: Deformation of topological particles

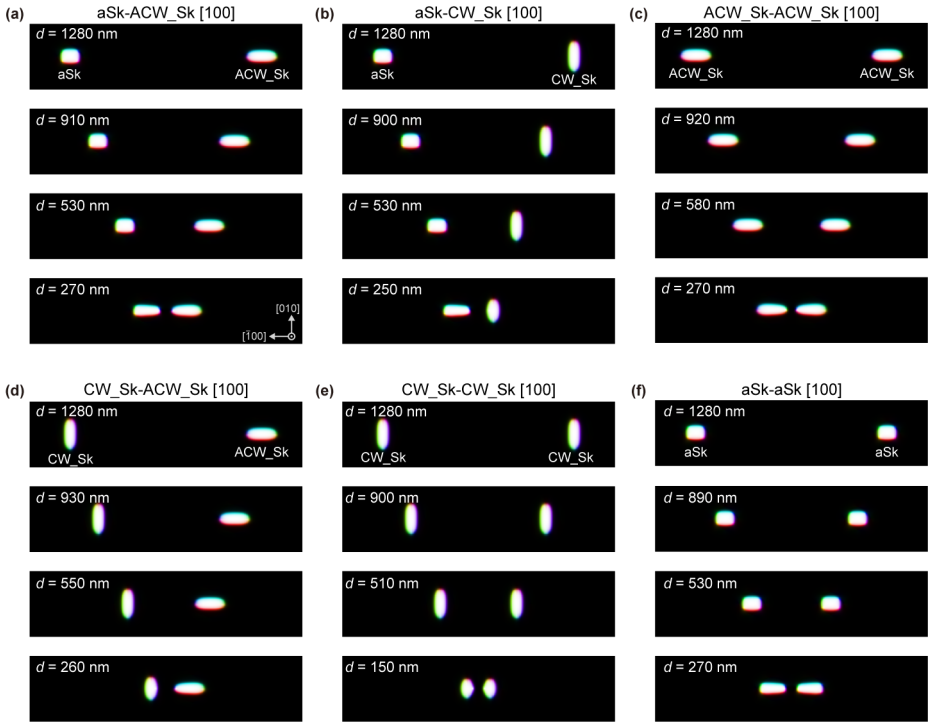

Figure S9. Magnetization distribution maps where the two topological particles are aligned along the [100] direction. All of the maps show the deformation of the topological particles.

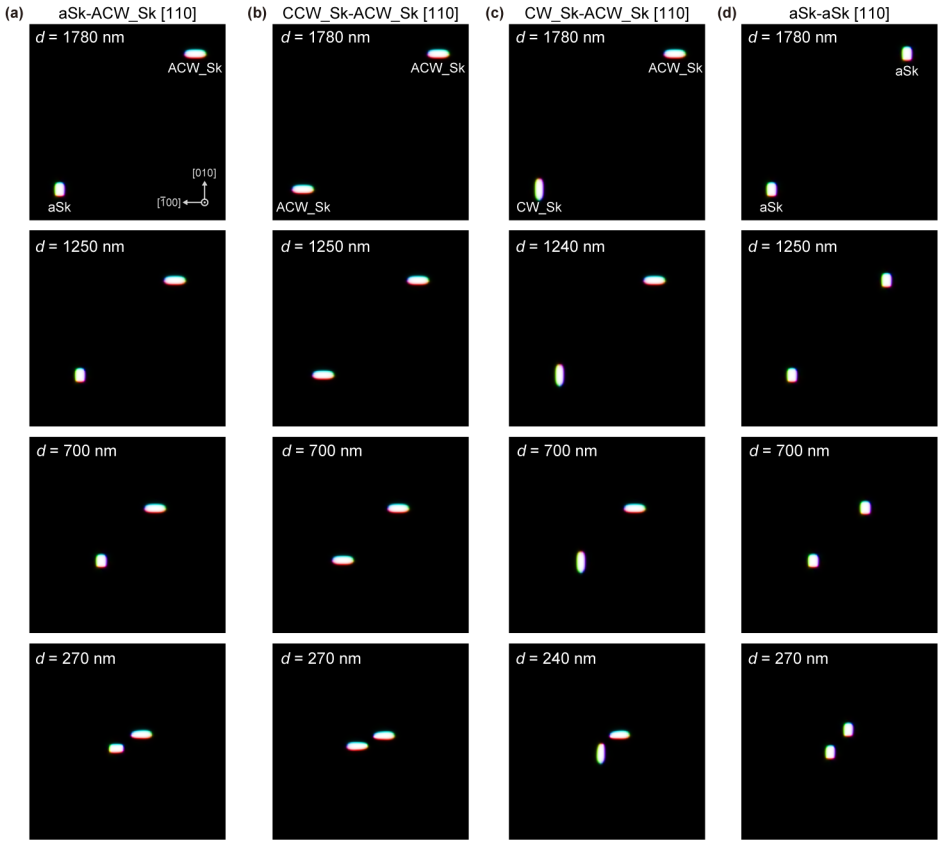

Figure S10. Magnetization distribution maps where the two topological particles are aligned along the [110] direction. All of the maps show the deformation of the topological particles.

X: Magnetic energy changes in every combination other than aSk-ACW_Sk[100] and aSk-aSk[100]

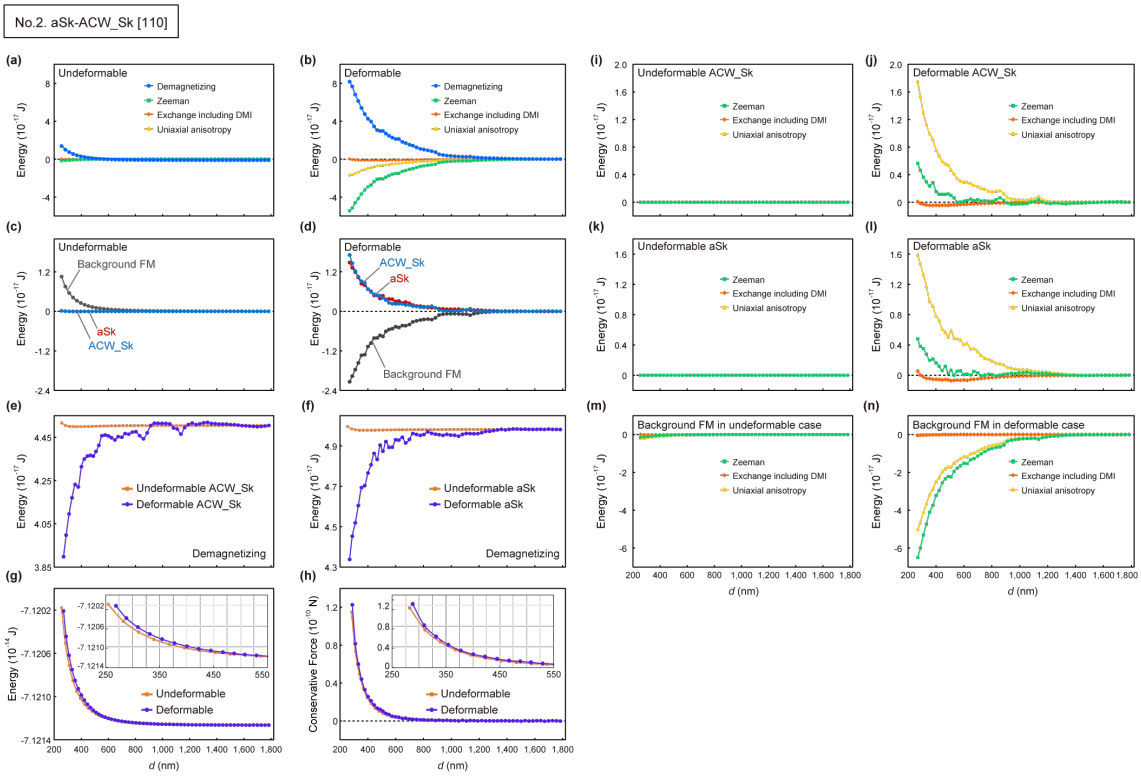

Figure S11. Simulated magnetic energy changes with decreasing *d* in aSk-ACW_Sk[110] (No. 2 in Table. S2). We compare the deformable to undeformable cases. (a),(b) Changes of the demagnetizing (blue), Zeeman (green), exchange including DMI (orange), and uniaxial anisotropy (yellow) energies for the undeformable (a) and deformable (b) cases. (c),(d) Energy changes of the skyrmion (blue), antiskyrmion (red), and background FM (gray) for the undeformable (c) and deformable (d) cases. Figures (a),(b),(c),(d) display the energy change from d = 1780 nm. (e),(f) Demagnetizing energy change of the ACW skyrmion (e) and antiskyrmion (f). The orange and purple lines are the undeformable and deformable cases, respectively. (g),(h) Total energy (g) and conservative force (h). The colored lines are the same meanings in (e),(f). Insets: Enlarged views below d = 550 nm. (i)-(n) Changes of the Zeeman (green), exchange including DMI (orange), and uniaxial anisotropy (yellow) energies for the undeformable (i) and deformable (j) ACW skyrmion, the undeformable (k) and deformable (l) antiskyrmion, and the background FM in the undeformable (m) and deformable (n) case.

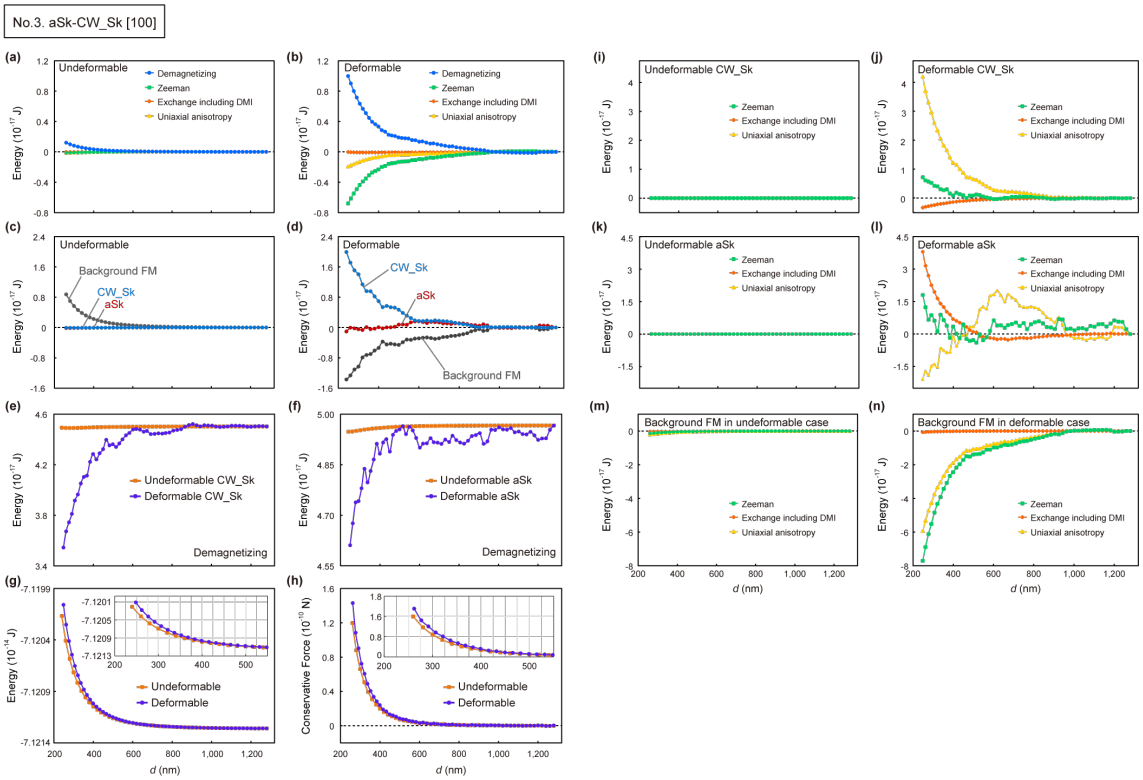

Figure S12. Simulated magnetic energy changes with decreasing *d* in aSk-CW_Sk[100] (No. 3 in Table. S2). We compare the deformable to undeformable cases. (a),(b) Changes of the demagnetizing (blue), Zeeman (green), exchange including DMI (orange), and uniaxial anisotropy (yellow) energies for the undeformable (a) and deformable (b) cases. (c),(d) Energy changes of the CW skyrmion (blue), antiskyrmion (red), and background FM (gray) for the undeformable (c) and deformable (d) cases. Figures (a),(b),(c),(d) display the energy change from d = 1780 nm. (e),(f) Demagnetizing energy change of the CW skyrmion (e) and antiskyrmion (f). The orange and purple lines are the undeformable and deformable cases, respectively. (g),(h) Total energy (g) and conservative force (h). The colored lines are the same meanings in (e),(f). Insets: Enlarged views below d = 550 nm. (i)-(n) Changes of the Zeeman (green), exchange including DMI (orange), and uniaxial anisotropy (yellow) energies for the undeformable (i) and deformable (j) CW skyrmion, the undeformable (k) and deformable (l) antiskyrmion, and the background FM in the undeformable (m) and deformable (n) case.

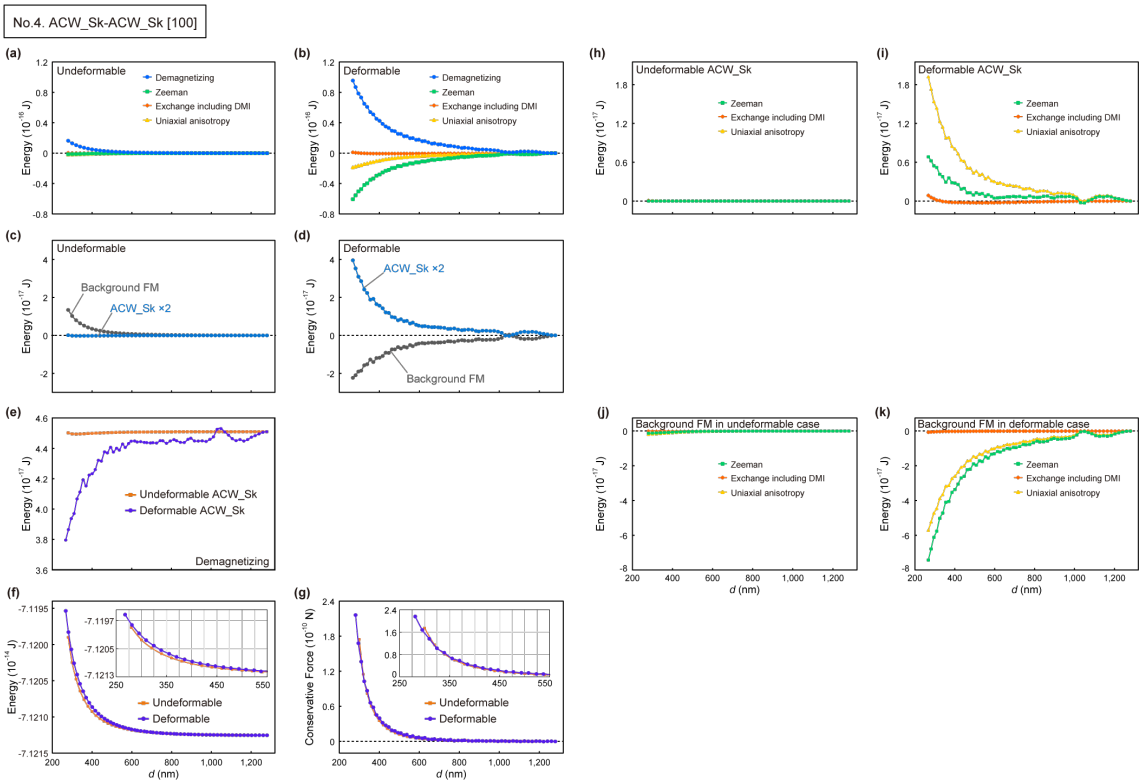

Figure S13. Simulated magnetic energy changes with decreasing *d* in ACW_Sk-ACW_Sk[100] (No. 4 in Table. S2). We compare the deformable to undeformable cases. (a),(b) Changes of the demagnetizing (blue), Zeeman (green), exchange including DMI (orange), and uniaxial anisotropy (yellow) energies for the undeformable (a) and deformable (b) cases. (c),(d) Energy changes of the ACW skyrmion (blue), and background FM (gray) for the undeformable (c) and deformable (d) cases. The two ACW skyrmions show the same energy behavior so that we display the sum of the energies of the two ACW skyrmions in (c),(d). Figures (a),(b),(c),(d) display the energy change from d = 1280 nm. (e) Demagnetizing energy change of the ACW skyrmion. The orange and purple lines are the undeformable and deformable cases, respectively. (f),(g) Total energy (f) and conservative force (g). The colored lines are the same meanings in (e). Insets: Enlarged views below d = 550 nm. (h)-(k) Changes of the Zeeman (green), exchange including DMI (orange), and uniaxial anisotropy (yellow) energies for the undeformable (h) and deformable (i) ACW skyrmion, and the background FM in the undeformable (j) and deformable (k) case.

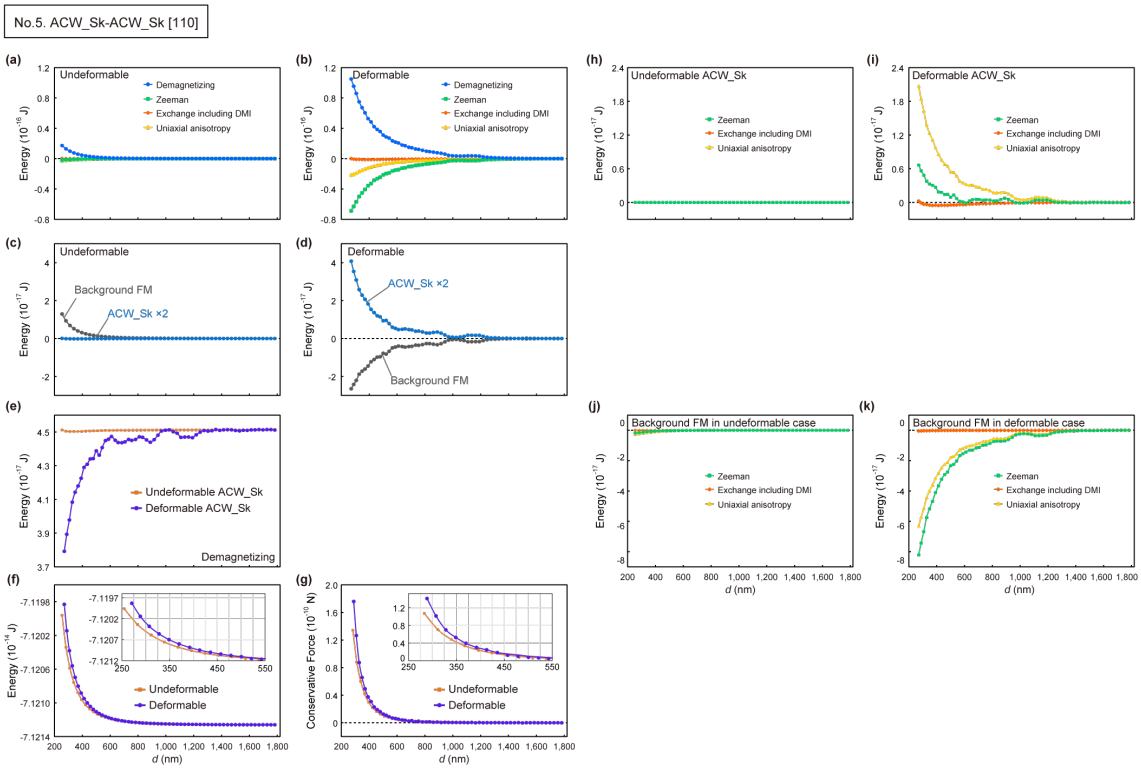

Figure S14. Simulated magnetic energy changes with decreasing d in ACW_Sk-ACW_Sk[110] (No. 5 in Table. S2). We compare the deformable to undeformable cases. (a),(b) Changes of the demagnetizing (blue), Zeeman (green), exchange including DMI (orange), and uniaxial anisotropy (yellow) energies for the undeformable (a) and deformable (b) cases. (c),(d) Energy changes of the two ACW skyrmions (blue), and background FM (gray) for the undeformable (c) and deformable (d) cases. The two ACW skyrmions show the same energy behavior so that we display the sum of the energies of the two ACW skyrmions in (c),(d). Figures (a),(b),(c),(d) display the energy change from d = 1780 nm. (e) Demagnetizing energy change of the ACW skyrmion. The orange and purple lines are the undeformable and deformable cases, respectively. (f),(g) Total energy (f) and conservative force (g). The colored lines are the same meanings in (e). Insets: Enlarged views below d = 550 nm. (h)-(k) Changes of the Zeeman (green), exchange including DMI (orange), and uniaxial anisotropy (yellow) energies for the undeformable (h) and deformable (i) ACW skyrmion, and the background FM in the undeformable (j) and deformable (k) case.

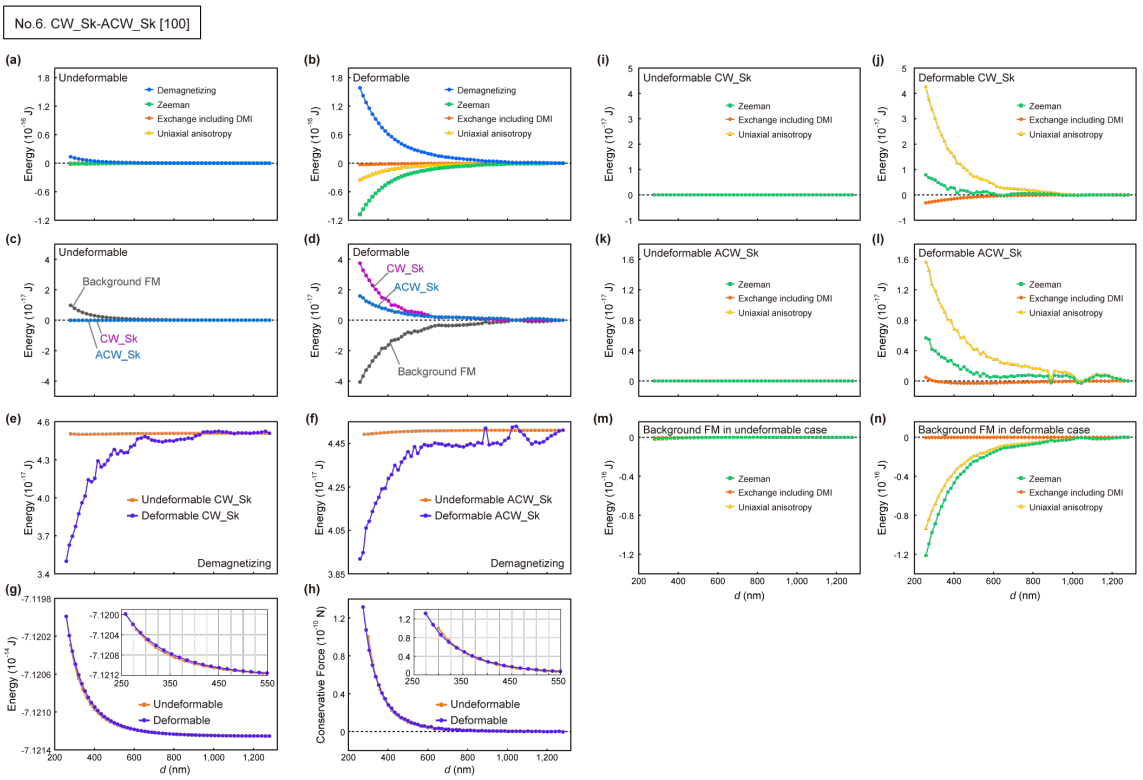

Figure S15. Simulated magnetic energy changes with decreasing *d* in CW_Sk-ACW_Sk[100] (No. 6 in Table. S2). We compare the deformable to undeformable cases. (a),(b) Changes of the demagnetizing (blue), Zeeman (green), exchange including DMI (orange), and uniaxial anisotropy (yellow) energies for the undeformable (a) and deformable (b) cases. (c),(d) Energy changes of the ACW skyrmion (blue), CW skyrmion (purple), and background FM (gray) for the undeformable (c) and deformable (d) cases. Figures (a),(b),(c),(d) display the energy change from d = 1280 nm. (e),(f) Demagnetizing energy change of the CW skyrmion (e) and ACW skyrmion (f). The orange and purple lines are the undeformable and deformable cases, respectively. (g),(h) Total energy (g) and conservative force (h). The colored lines are the same meanings in (e),(f). Insets: Enlarged views below d = 550 nm. (i)-(n) Changes of the Zeeman (green), exchange including DMI (orange), and uniaxial anisotropy (yellow) energies for the undeformable (i) and deformable (j) CW skyrmion, the undeformable (k) and deformable (l) ACW skyrmion, and the background FM in the undeformable (m) and deformable (n) case.

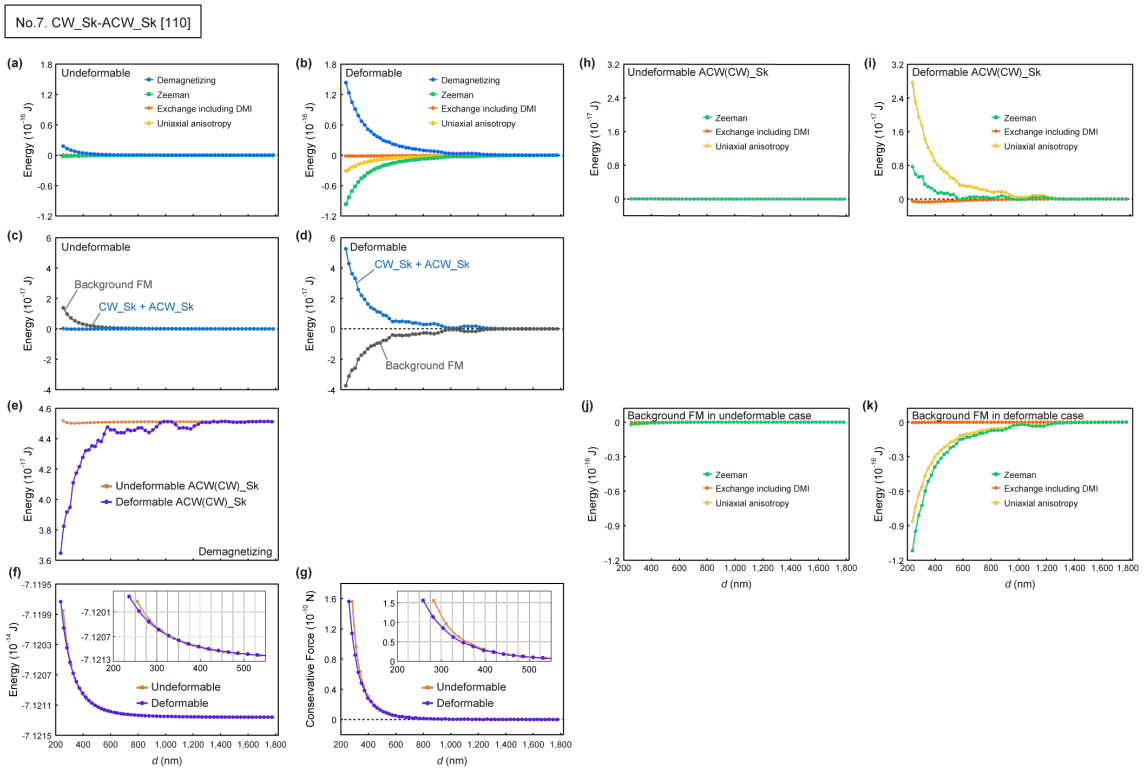

Figure S16. Simulated magnetic energy changes with decreasing *d* in CW_Sk-ACW_Sk[110] (No. 7 in Table. S2). We compare the deformable to undeformable cases. (a),(b) Changes of the demagnetizing (blue), Zeeman (green), exchange including DMI (orange), and uniaxial anisotropy (yellow) energies for the undeformable (a) and deformable (b) cases. (c),(d) Energy changes of the ACW skyrmion + CW skyrmion (blue), and background FM (gray) for the undeformable (c) and deformable (d) cases. The energy behaviors of the ACW skyrmion are in quantitative agreement with those of the CW skyrmion so that we display the sum of the energies of the ACW skyrmion and CW skyrmions in (c),(d). Figures (a),(b),(c),(d) display the energy change from d = 1780 nm. (e) Demagnetizing energy change of the ACW (CW) skyrmion. The orange and purple lines are the undeformable and deformable cases, respectively. (f),(g) Total energy (f) and conservative force (g). The colored lines are the same meanings in (e). Insets: Enlarged views below d = 550 nm. (h)-(k) Changes of the Zeeman (green), exchange including DMI (orange), and uniaxial anisotropy (yellow) energies for the undeformable (h) and deformable (i) ACW (CW) skyrmion, and the background FM in the undeformable (j) and deformable (k) case.

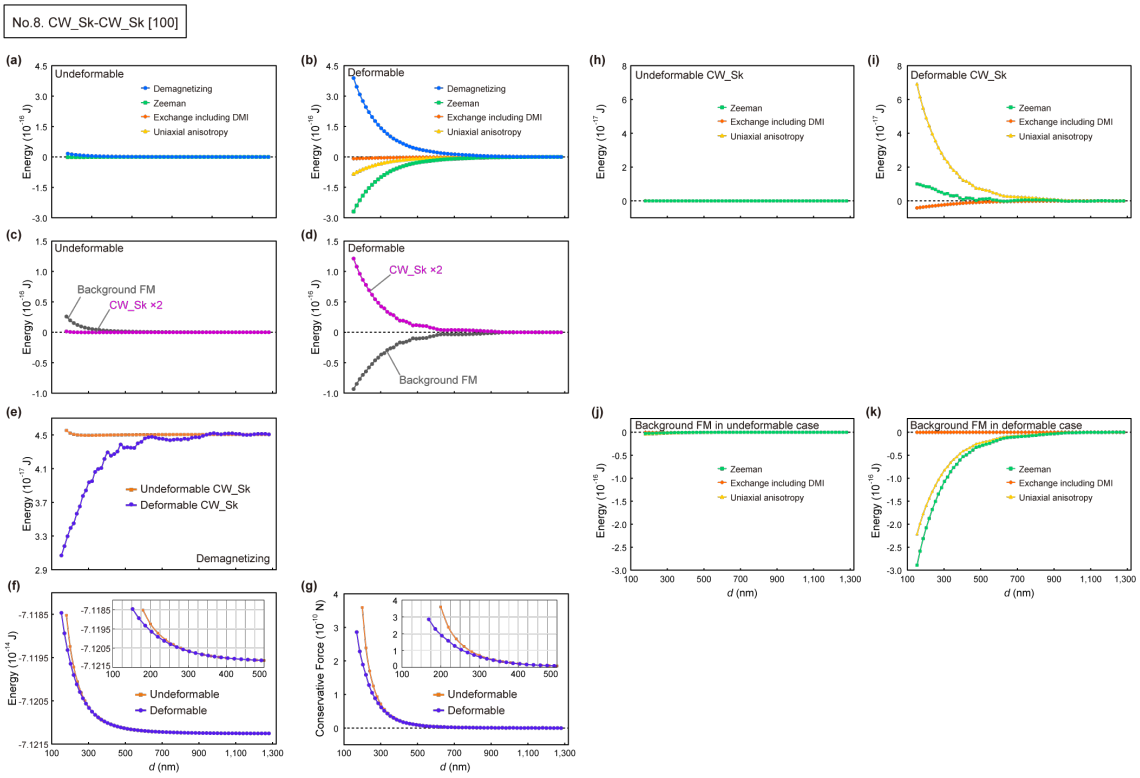

Figure S17. Simulated magnetic energy changes with decreasing d in CW_Sk-CW_Sk[100] (No. 8 in Table. S2). We compare the deformable to undeformable cases. (a),(b) Changes of the demagnetizing (blue), Zeeman (green), exchange including DMI (orange), and uniaxial anisotropy (yellow) energies for the undeformable (a) and deformable (b) cases. (c),(d) Energy changes of the two CW skyrmions (purple), and background FM (gray) for the undeformable (c) and deformable (d) cases. The two CW skyrmions show the same energy behavior so that we display the sum of the energies of the two CW skyrmions in (c),(d). Figures (a),(b),(c),(d) display the energy change from d = 1280 nm. (e) Demagnetizing energy change of the CW skyrmion. The orange and purple lines are the undeformable and deformable cases, respectively. (f),(g) Total energy (f) and conservative force (g). The colored lines are the same meanings in (e). Insets: Enlarged views below d = 500 nm. (h)-(k) Changes of the Zeeman (green), exchange including DMI (orange), and uniaxial anisotropy (yellow) energies for the undeformable (h) and deformable (i) CW skyrmion, and the background FM in the undeformable (j) and deformable (k) case.

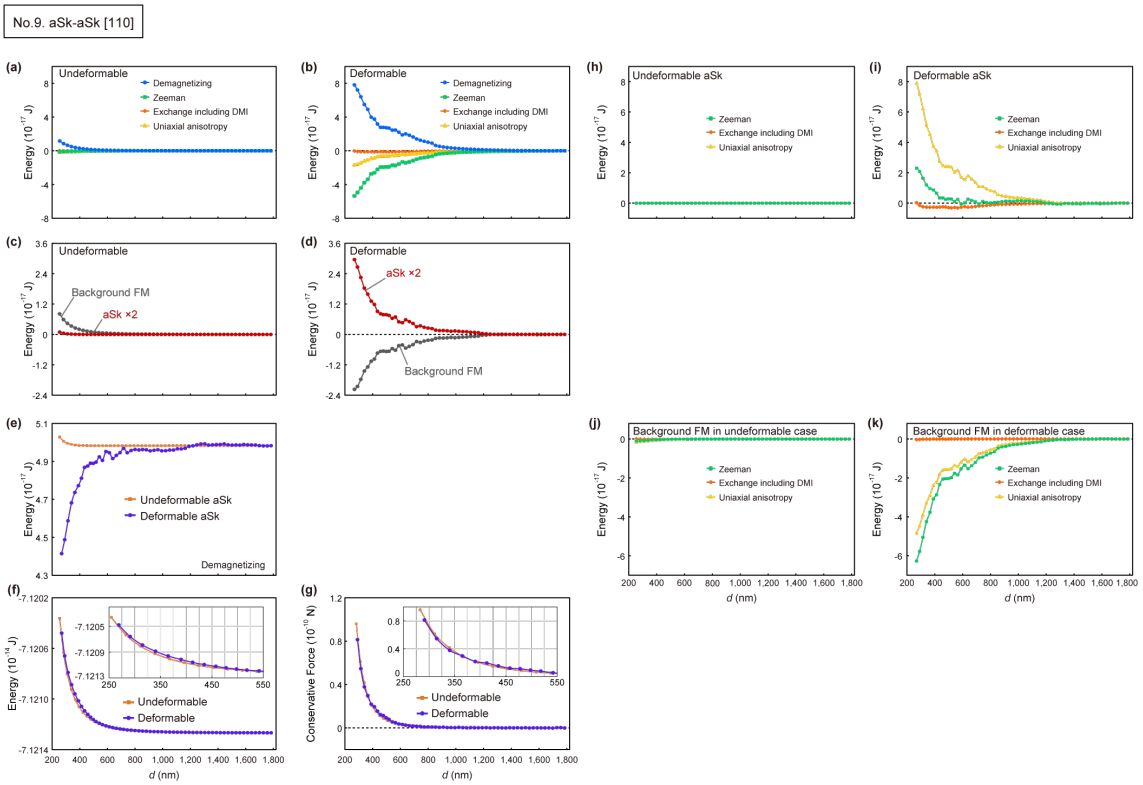

Figure S18. Simulated magnetic energy changes with decreasing d in aSk-aSk[110] (No. 9 in Table. S2). We compare the deformable to undeformable cases. (a),(b) Changes of the demagnetizing (blue), Zeeman (green), exchange including DMI (orange), and uniaxial anisotropy (yellow) energies for the undeformable (a) and deformable (b) cases. (c),(d) Energy changes of the two antiskyrmions (red), and background FM (gray) for the undeformable (c) and deformable (d) cases. The two antiskyrmions show the same energy behavior so that we display the sum of the energies of the two antiskyrmions in (c),(d). Figures (a),(b),(c),(d) display the energy change from d = 1780 nm. (e) Demagnetizing energy change of the antiskyrmion. The orange and purple lines are the undeformable and deformable cases, respectively. (f),(g) Total energy (f) and conservative force (g). The colored lines are the same meanings in (e). Insets: Enlarged views below d = 550 nm. (h)-(k) Changes of the Zeeman (green), exchange including DMI (orange), and uniaxial anisotropy (yellow) energies for the undeformable (h) and deformable (i) antiskyrmion, and the background FM in the undeformable (j) and deformable (k) case.

XI: Magnetic energy changes in aSk-aSk[100] and magnetic flux density map

The magnetic energy behaviors in aSk-aSk[100] is different from those of the other combinations, as shown in Figure S19.

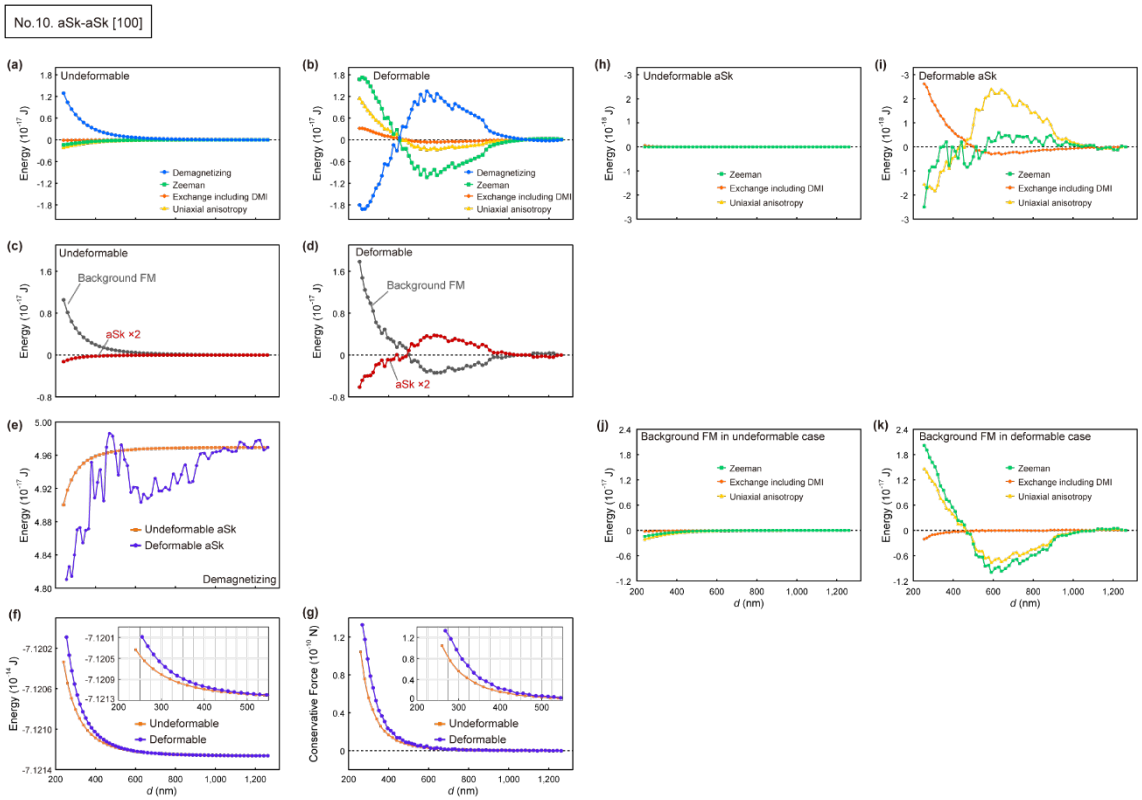

Figure S19. Simulated magnetic energy changes with decreasing *d* in aSk-aSk[100] (No. 10 in Table. S2). We compare the deformable to undeformable cases. (a),(b) Changes of the demagnetizing (blue), Zeeman (green), exchange including DMI (orange), and uniaxial anisotropy (yellow) energies for the undeformable (a) and deformable (b) cases. (c),(d) Energy changes of the two antiskyrmions (red), and background FM (gray) for the undeformable (c) and deformable (d) cases. The two antiskyrmions show the same energy behavior so that we display the sum of the energies of the two antiskyrmions in (c),(d). Figures (a),(b),(c),(d) display the energy change from $d = 1280$ nm. (e) Demagnetizing energy change of the antiskyrmion. The orange and purple lines are the undeformable and deformable cases, respectively. (f),(g) Total energy (f) and conservative force (g). The colored lines are the same meanings in (e). Insets: Enlarged views below $d = 550$ nm. (h)-(k) Changes of the Zeeman (green), exchange including DMI (orange), and uniaxial anisotropy (yellow) energies for the undeformable (h) and deformable (i) antiskyrmion, and the background FM in the undeformable (j) and deformable (k)

case.

The transport of intensity equation (TIE) analysis using L-TEM images to visualize in-plane magnetic flux density has been powerful in studying magnetic skyrmions.[8] However, magnetic flux density outside a skyrmion generated by the skyrmion, which is the sum of demagnetization flux density inside the thin film and leakage magnetic flux density outside the thin film, are so weak that they have never been visualizable. The exception is an antiskyrmion where magnetic flux density can be observed in its close vicinity[2,9] due to its unique magnetic structure. We have visualized magnetic flux density (demagnetizing fields) that smoothly connects the antiskyrmion spin structure situated close to each other along with the <100> directions in a square antiskyrmion lattice, as shown in Figure S20. Therefore, the difference in magnetic energy behaviors of aSk-aSk[100] from the other combinations may originate from the unique magnetic structure of antiskyrmions.

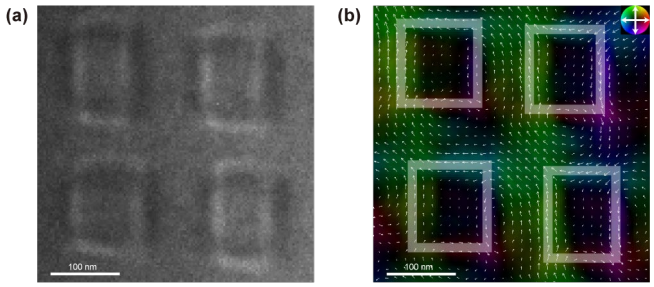

Figure S20. L-TEM image and corresponding in-plane magnetic flux density map of a square antiskyrmion lattice. (a) An underfocused L-TEM image of the square antiskyrmion lattice. (b) In-plane magnetic flux density map using the TIE analysis based on underfocused (a) and overfocused L-TEM images. Closed white lines are the outlines of antiskyrmions. The colors and arrows indicate the direction and magnitude of the magnetic flux density as referred to in the inset color wheel. The map allows us to see the magnetic flux density outside the magnetizations of antiskyrmions, of which a portion smoothly connects between antiskyrmions.

Reference

[1]. Ma, T.; Sharma, A. K.; Saha, R.; Srivastava, A. K.; Werner, P.; Vir, P.; Kumar, V.; Felser, C.; Parkin, S. S. P. Tunable Magnetic Antiskyrmion Size and Helical Period from Nanometers to Micrometers in a D_{2d} Heusler Compound. *Adv. Mater*. **2020**, 32 (28), 2002043.

[2]. Peng, L.; Takagi, R.; Koshibae, W.; Shibata, K.; Nakajima, K.; Arima, T.; Nagaosa, N.; Seki, S.; Yu, X. Z.; Tokura, Y. Controlled transformation of skyrmions and antiskyrmions in a non-centrosymmetric magnet. *Nat. Nanotechnol*. **2020**, 15 (3), 181–186.

[3]. Koshibae, W.; Nagaosa, N. Creation of skyrmions and antiskyrmions by local heating. *Nat. Commun*. **2014**, 5, 5148.

[4]. Kong, L.; Zang, J. Dynamics of an Insulating Skyrmion under a Temperature Gradient. *Phys. Rev. Lett*. **2013**, 111 (6), 067203.

[5]. Jiang, W.; Upadhyaya, P.; Fan, Y.; Zhao, J.; Wang, M.; Chang, L.-T.; Lang, M.; Wong, K. L.; Lewis, M.; Lin, Y.-T.; Tang, J.; Cherepov, S.; Zhou, X.; Tserkovnyak, Y.; Schwartz, R. N.; Wang, K. L. Direct Imaging of Thermally Driven Domain Wall Motion in Magnetic Insulators. *Phys. Rev. Lett.* **2013**, 110 (17) 177202.

[6]. Mochizuki, M.; Yu, X. Z.; Seki, S.; Kanazawa, N.; Koshibae, W.; Zang, J.; Mostovoy, M.; Tokura, Y.; Nagaosa, N. Thermally Driven Ratchet Motion of a Skyrmion Microcrystal and Topological Magnon Hall Effect. *Nat. Mater*. **2014**, 13, 241– 246.

[7]. Wang, Z.; Guo, M.; Zhou, H.-A.; Zhao, L.; Xu, T.; Tomasello, R.; Bai, H.; Dong, Y.; Je, S.-G.; Chao, W.; Han, H.-S.; Lee, S.; Lee, K.-S.; Yao, Y.; Han, W.; Song, C.; Wu, H.; Carpentieri, MG. Finocchio,G.; Im, M.-Y.; Lin, S.-Z; Jiang, W.; Thermal generation, manipulation and thermoelectric detection of skyrmions. *Nat. Electron*. **2020**, 3, 672–679.

[8]. Ishizuka, K.; Allman, B. Phase Measurement of Atomic Resolution Image Using Transport of Intensity Equation. *Microscopy* **2005**, 54 (3), 191– 197.

[9]. Karube, K.; Peng, L.; Masell, J.; Yu, X. Z.; Kagawa, F.; Tokura, Y.; Taguchi, Y. Room-temperature antiskyrmions and sawtooth surface textures in a non-centrosymmetric magnet with S_4 symmetry. *Nat. Mater*. **2021**, 20 (3), 335–340.